Effect of Annealing Temperature on the Structural and Optical Characteristics of Cobalt Doped Zinc Oxide

By

SAHAANA B

(Reg. No. 21PPH016)

Supervisor

Dr. N. S. Rajeswari

Department of Physics

A Thesis Submitted to

Avinashilingam Institute for Home Science and Higher Education for Women

Coimbatore - 641043

In partial fulfilment of the requirements for the degree of

MASTER OF SCIENCE IN PHYSICS

MAY 2023

Effect of Annealing Temperature on the Structural and Optical Characteristics of Cobalt Doped Zinc Oxide

By

SAHAANA B

(Reg. No. 21PPH016)

Supervisor

Dr. N. S. Rajeswari

Department of Physics

A Thesis submitted to

Avinashilingam Institute for Home Science and Higher Education for Women

Coimbatore – 641043

In partial fulfilment of the requirement for the degree of

MASTER OF SCIENCE IN PHYSICS

MAY 2023

CERTIFIED AS A BONAFIDE RESEARCH WORK

12/05/23

Signature of Head of the Department

Dr. J. SHANTHI, M.Sc., M.Phil., Ph.D.,
Professor and Head
Department of Physics
Avinashilingam Institute for Home Science
and Higher Education For Women
Coimbatore - 641 043.

12/5/2023

Signature of the Supervisor

ACKNOWLEDGEMENT

I owe my sincere thanks to the Lord Almighty and My Parents without whom I would have been nothing and showering their blessings upon me in all my endeavours.

I wish to express my deep sense of reverential gratitude to **Prof. S. P. Thyagarajan**, Chancellor, Avinashilingam Institute for Home Science and Higher Education for Women, Coimbatore for all the good wishes towards the completion of the study.

I extend my sincere thanks to **Dr. (Mrs.) V. Bharathi Harishankar** Chancellor, Avinashilingam Institute for Home Science and Higher Education for Women, Coimbatore for her encouragement towards the academic performance.

I wish to express my deep sense of gratitude to **Dr.(Mrs.) S. Kowsalya**, Registrar, Avinashilingam Institute for Home Science and Higher Education for Women, Coimbatore for her moral support and help for my study.

I wish to express my gratitude to **Dr.(Mrs.) G. Padmavathi**, Dean, School of Physical Sciences and Computational Sciences, Avinashilingam Institute for Home Science and Higher Education for Women, Coimbatore for her positive advice and generous help.

I wish to express my deep sense of gratitude to **Dr.(Mrs.) J. Shanthi**, Professor and Head, Department of Physics, Avinashilingam Institute for Home Science and Higher Education for Women, Coimbatore for her encouragement to complete my study.

I express my sincere gratitude to my guide **Dr.(Mrs.) N. S. Rajeswari**, Assistant Professor (S.G), Department of Physics, Avinashilingam Institute for Home Science and Higher Education for Women, Coimbatore for her excellent guidance, constant encouragement, valuable advice and moral support throughout the study.

I sincerely thank **all other Staff Members** of the **Department of Physics**, Avinashilingam Institute for Home Science and Higher Education for Women, Coimbatore for being supportive on all our activities.

I am thankful to Research Scholar **Ms. P. Mehana** for her constant support for successfully completing the project work and special word of thanks to **Ms. R. Dhivyaprabha,** II M.Sc., Department of Physics.

I would like to express my thanks to **all my friends** and **my family members** for their support throughout my study and help in carrying out this work successfully.

SAHAANA B

CONTENTS

LIST OF TABLES

LIST OF FIGURES

CHAPTER I

INTRODUCTION

1.1. Semiconductors

Semiconductors are crystalline solids with electrical conductivities that lie between the properties of insulators and conductors. Semiconductors are pure materials but sometimes impurities are added to increase their degree of conductivity. Chemically processing of such materials can enable the transmission and control of an electric current. At very low temperatures, a semiconductor acts as an insulator, but as temperature increases, so does its electrical conductivity. A semiconductor has weaker conductivity than a conductor even at room temperature. Compound semiconductors like gallium arsenide, elemental materials like silicon, or alloys like silicon germanium or aluminium gallium arsenide can all be used as semiconductors. The conductivity and other electrical properties of semiconductors are determined by the material's electronic band structure. By adding impurities, it will modify the semiconductor's electrical properties and this procedure is known as doping. Electronic devices of all kinds, such as diodes, transistors, and integrated circuits, are developed with the help of semiconductors. Due to their flexibility, durability, power efficiency, and low price, such systems have found extensive use. Moreover, externally applied electrical or magnetic fields can affect the semiconductor's electronic characteristics. Devices like Hall effect sensors and insulated-gate field effect transistors (IGFETs or MOSFETs) are mainly successful in this phenomenon. Semiconductors handle a wide range of current and voltage, and more importantly, it is well suitable for integration into complex but easily produced microelectronic circuits [1].

According to the number of elements, this is classified into two types:

- Elemental semiconductors: These semiconductors are made of a single element.
  Example: Si and Ge.
- Compound semiconductors: These semiconductors are made from two or more elements.
  Example: GaAs, GaN, SiC

1.2. Band Theory of Semiconductors

1.2.1. Bands Concept

The combination of molecular orbitals that are close in energy results in continuous band energy. Bands with different energies will probably form as a result of the mass balances of the various molecular orbit mixings. The energy difference between the top of the valence band and the bottom of the conduction band is called band gap and electrons can jump from one band to another. The band gap energy is the minimal amount of energy required for an electron to shift from a valence band to a conduction band. In the semiconductor and nanomaterials fields, band gap measurement is important. Insulators have a high band gap energy (>3 eV), whereas semiconductors have a smaller band gap energy (3 eV).

According to Bohr's hypothesis, each atom's shell has a varied quantity of energy at a distinct position. The main target of this theory is to transmit electron between the inner and outer shells. The energy band is classified into three different categories based on the theory of energy bands,

- Conduction Band (CB)
- Valence Band (VB)
- Forbidden Gap

1.2.1.1. Conduction Band

At normal temperature, the valence electrons are loosely connected to the nucleus. Some valence electrons, electrons will be able to depart the band freely. Because the flow towards neighbouring atoms, these are called free electrons. These free electrons, are known as conduction electrons, will conduct current flow within a conductor and its occupied energy is lower.

1.2.1.2. Valence Band

Electron travel at fixed energy levels within atoms, the energy of an electron in the inner shell is greater than that of an electron in the outer shell. The electrons that are located within the outer shell are known as valence electron. These electrons are made up of a series of energy levels that make up the valence band. This band has the highest level of occupied energy.

1.2.1.3. Forbidden Gap

The prohibited gap is defined as the space between the conduction and valence bands. This is a band that is not allowed to exist because it lacks energy. As a result, no electrons flow in this band. This gap will allow electrons to move from the valence to the conduction state. The electron in the valence band are tightly linked to the nucleus if this gap is larger. At the moment, a little external force is required to push the electrons out of this band [2].

1.3. Band gap theory of semiconductor

According to the band theory, semiconductors will behave as insulators at absolute zero. The metal would behave as a semiconductor if it were above room temperature and maintained below the solids melting point. Semiconductors are classified into different types based on the completely occupied valance and unoccupied conduction bands. The electrons must be excited to move from the VB to the CB, due to the narrow band gap between these two bands. In semiconductors, the CB is fully empty, while the VB is electron-filled. The energy gap between the upper level of VB and the lower level of CB is called the forbidden gap or bandgap (E_g). An electron is excited from VB to CB by photo-irradiations of energy equal to or greater than bandgap energy. The excitation energy for an electron moving from VB to CB depends on the bandgap, which differs for different semiconductors. However, the CB is partially filled which allows the electron to move freely through the semiconductor lattice resulting in the vacancy created due to the excitation of an electron that can move freely in the VB and which is partially filled [3].

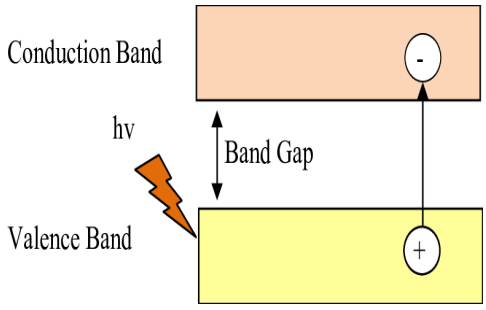

Fig. 1.1 Conduction, Valence bands and electron-hole pair generation in semiconductor

1.4. Types of semiconductors

According to the purity, semiconductors are classified into two main classes:

- Intrinsic semiconductor (or pure)
- Extrinsic semiconductor (or impure)

1.4.1. Intrinsic Semiconductor

A semiconductor in which holes and electrons are created purely by thermal excitation across the energy gap is known as an intrinsic semiconductor. These types of semiconductors have no impurity type or imperfection but may have defects. Germanium and silicon in pure form are two examples of intrinsic semiconductors. In these cases, there are four nearest neighbours to each atom and there are two electron bonds between each of the nearest and the atom. In an intrinsic semiconductor, a forbidden gap exists between a filled valence band and the conduction band, but the width of the forbidden gap conveyed in energy is much smaller than that of an insulator. Due to the thermal excitation of electrons from the valence to the conduction band, there is conduction occurs in this type of semiconductor. The electron extending conduction band due to thermal excitation leave an equal number of vacancies or holes in the valence band is an intrinsic semiconductor. The concentration of holes and electrons must be always the same. Intrinsic semiconductors only have limited applications. They are neither good conductor nor insulators, and their conduction is primarily temperature dependent.

1.4.2. Extrinsic Semiconductor

When impurity atoms are comprised into a pure semiconductor crystal then its electrical properties are changed. A material most of whose charge carriers arise from impurity atoms is called an impurity semiconductor. The balance of electron and hole densities is perturbed by adding impurity atoms to a pure semiconductor crystal (concentration becomes unequal). When a bandgap is specifically adding small impurities to the material the process is said to be Doping and the impurity atoms are called dopants. The dopant must be chosen to prevent distortion of the semiconductor lattice. It occupies only a small number of the semiconductor atom sites in the crystal the size of the semiconductor atoms and the dopant atoms should be nearly equal [4].

There are two types of dopants used in doping the tetravalent Si or Ge:

- pentavalent (Valency 5); like Arsenic (As), Antimony (Sb), Phosphorous (P), etc.
- Trivalent (Valency 3); like Indium (In), Boron (B), Aluminium (Al), etc.

The reason behind using these dopants is to have identical-sized atoms as the pure semiconductor. Si and Ge both belong to the fourth group of the periodic table. Hence, the option of the dopants is from the third and fifth groups. As a result, the atom sizes are maintained relatively close to those of the fourth group. Therefore, the trivalent and pentavalent choices are the by-product. Two different classes of semiconductors are formed by these dopants:

- n-type semiconductor
- p-type semiconductor

n-type semiconductor

Doping pentavalent elements into pure semiconductors like Si and Ge results in the formation of an n-type semiconductor.

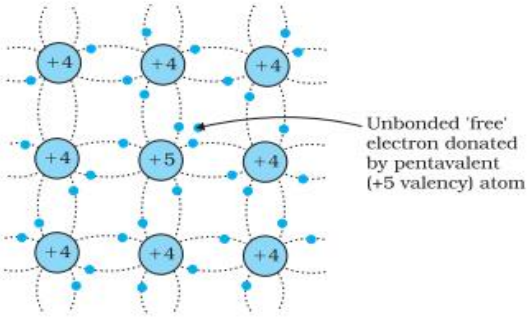

Fig. 1.2 Schematic representation of doping in n- type semiconductor

When the pentavalent atom replaces a Si atom, four of its electrons form bonds with the four Si atoms located near the area. Consequently, the fifth electron is still loosely bonded to the parent atom. The ionization energy required to remove this electron free is very small. Because of this, the electron can move within the lattice even at room temperature. For example, silicon requires about 1.1 eV of energy to ionize when it is at room temperature. On other hand, this energy decreases to about 0.05 eV when a pentavalent impurity is added.

The number of electrons that dopant atoms release is mainly controlled by the doping level and independent of the ambient temperature. The Si atoms also release some electrons

and produce some holes as the temperature rises. However, the number of these holes is very small. Hence, the number of free electrons is always much higher than the number of holes. Therefore, the recombination also results in a reduction in the number of holes. Electrons constitute majority charge carriers when a pentavalent atom is doped into a semiconductor. On the other hand, the minority charge carriers are the holes. These extrinsic semiconductors are n-type semiconductors.

For n-type semiconductors,

Number of free electrons (n_e) >> Number of holes (n_h)

p-type semiconductor

Doping pure semiconductors like Si and Ge with trivalent elements results in the formation of a p-type semiconductor. When a trivalent atom takes the place of a Si atom, three of its electrons bond with three nearby Si atoms. There is no electron to bond with the fourth Si atom. As a consequence, this creates a vacancy or hole between the trivalent and fourth silicon atom. To fill the vacancy, an electron must jump from the atom's outer orbit in the neighborhood region. This creates a hole in the site from where the electron jumps. It is simply said to be a hole that is now available for conduction.

The number of holes created by the dopant atoms is strongly influenced by the doping level and independent of the surrounding temperature. As well as the temperature increases, the Si atoms free some electrons and generate some holes. However, there a very few of these electrons in existence. Therefore, the number of holes is always much greater than the number of free electrons. Therefore, the number of free electrons decreased because of recombination. Holes act as the majority charge carriers in a semiconductor when it is doped with a trivalent atom. By comparison, the minority of charge carriers are free electrons. Such extrinsic semiconductors are called p-type semiconductors.

For p-type semiconductors,

Number of holes (n_h) >> Number of free electrons (n_e) [5].

1.5. Difference between an intrinsic and extrinsic semiconductor

Factors	Intrinsic semiconductor	Extrinsic semiconductor
Impurity in the material	These are pure forms of semiconductors, hence not have a significant amount of impurity	These are made by adding some impurity to the pure form of semiconductors
Density of electrons	The density of electrons is equal to the density of holes	The density of an electron is not equal to the density of holes
Electrical conductivity	It exhibits poor electrical conductivity	Electrical conductivity is significantly higher compared to an intrinsic semiconductor
Position in Fermi level	The Fermi energy level lie in the middle of the valence and conduction band	The Fermi level shifts towards the valence or conduction band
Temperature effect	Dependent on temperature	Dependent on the temperature as well as on the amount of impurity

Table 1.1 Comparison between intrinsic and extrinsic semiconductors

1.6. Energy Band Gaps and its types

The band gap of a semiconductor can be classified into two types based on the semiconductor physics, a direct band gap or an indirect band gap. For a conduction band, there is a minimum amount of energy state is present. On the other hand, the valance band requires a maximum amount of energy state. These bands are identified by a certain crystal momentum or k-vectors in the limited zone called the Brillouin zone. If the k-vectors are distinct, then the material has an indirect gap. If the crystal momentum of electrons and holes are the same in both the conduction band and the valence band then the band gap is said to be a direct band gap. In this band gap light or a photon can emit directly by an electron. But in an indirect gap, a photon cannot be emitted simply because the electron must pass through a transitional state and has to pass momentum to the crystal lattice.

Examples:

- Direct bandgap materials are amorphous silicon and the III-V materials like GaAs and InAs.
- Indirect bandgap materials consist of crystalline silicon and Ge. Some of the III-V materials include indirect bandgap such as AlSb [6].

1.6.1. Direct and indirect band gap semiconductors

Direct band gap

The band gap describes the minimum energy difference between the edge of the valence band and the bottom of the conduction band. The top of the valence band and the bottom of the conduction band, are commonly not at the same electron momentum value. The top edge of the valence band and the bottom of the conduction band in the direct band gap semiconductor occur at the same value of momentum which is shown in the Fig. 1.3 below

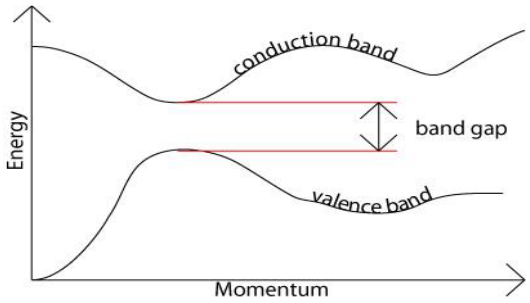

Fig. 1.3 Direct band gap semiconductor

In this, electrons can directly excite or de-excite by the absorption or emission of photons and there is no phonon involvement in the process of excitation and de-excitation. An electron in the valance band will absorb energy from a photon incident hν, $h\nu > E_g$, on it and then be excited to the conduction band. When it de-excites to the valance band, it will then emit some energy i.e. $h\nu = E_g$. Direct band semiconductors are used in light-emitting applications like LED.

Indirect band gap

In an indirect band gap semiconductor, the conduction bands require minimum energy that differs from the maximum energy in the valence band at a specified momentum

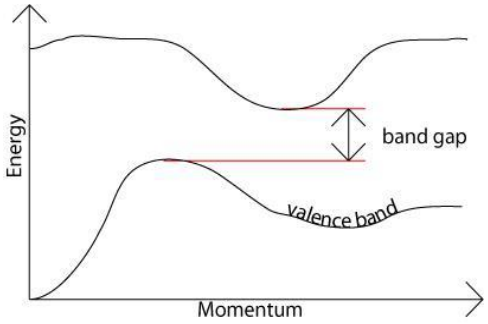

Fig. 1.4 Indirect band gap semiconductor

Here the phonon gets involved in the process of conservation for both momentum and energy. If the electron de-excites, some of the energy is transferred to the lattice and released as phonons, which creates the lattice to vibrate and release heat. This is distinct form the full quantity of energy being ejected as photons. As a result, light emission cannot be obtained with indirect band gap semiconductors. Example: Si, Ge, SiC, etc., [7].

1.7. Determination of the bandgap using Tauc plot

The energy required to excite an electron from the valance band to the conduction band is referred to as a semiconductors band gap energy. By determining the photophysical and photochemical properties of semiconductors requires an accurate estimation of the bandgap energy. In 1966, Tauc proposed a technique for determining an amorphous semiconductor's band gap energy using optical absorption spectra.

The Tauc method is based on the assumption that the energy-dependent absorption coefficient (α) and incident photon energy (hν) can be expressed by the following equation,

$$(\alpha.h\nu)^{n} = B\,(h\nu - E_g)$$

where B is the energy independent constant, E_g is the optical band gap energy of the material, n is the nature of transition, and ν is the frequency of the incident radiation. The above equation is known as Tauc and Devis-Mott relation. This relation is used to probe the optical band gap energy of particles from UV-vis absorption spectroscopy. The n factor depends on the mechanism of the electron transition and is equal to ½ or 2 for the direct and indirect transition band gaps, respectively. Diffuse reflectance spectra (DRS) are typically used to determine the band gap energy [8].

1.8. Photocatalysis : An Introduction

During the last few years, photocatalysis has expanded in both technological and commercial relevance. Nanotechnology developments have been significantly linked to photocatalytic performance enhancement. Photocatalyst is a versatile method that may be used to achieve a variety of goals, including the breakdown of various organic pollutants in wastewater, the production of hydrogen, air purification, and antibacterial activity. Compared to other studies, photocatalysis is fast developing and gaining attention from researchers due to various advantages such as low cost and attractive efficiency. It is a unique way to address energy and environmental issues. Photocatalysis is one of the innovative oxidation techniques used to degrade organic pollutants. In the photocatalytic method, several chalcogenides (oxides such as TiO_2, ZnO, ZrO_2, CeO_2, etc, or sulphides such as CdS, ZnS, etc.) have been used as photocatalysts and the method has been proven to be suitable for a wide range of organic pollutant for decolorization and degradation of organic pollutants [9].

The term photocatalysis refers to a chemical reaction generated by the absorption of UV (wavelength 100-400 nm), visible light (400-750 nm), and infrared radiation (750-2500 nm). In the overall reaction, a catalyst neither changes nor consumed. The photocatalyst activity (PCA) depends on the ability of catalyst to create hole-electron pairs that generate free radicals (OH-). Photocatalysis is the concurrent use of light and catalyst to support or enhance a chemical reaction. As a result, photocatalysis is described as the "catalysis-driven acceleration of a light-induced reaction". The basic principle of photocatalysis is that under UV light irradiation, organic molecules come into contact with the surface of the photocatalyst producing a series of oxidation and reduction (redox) reactions to occur. At least two simultaneous reactions must occur during this process: oxidation from the photogenerated hole and reduction from photogenerated electrons. The degradation of the resistant substance is caused by the formation of reactive hydroxyl radicals [10].

1.9. Environmental pollution

Ion exchange, adsorption process, membrane process, advanced oxidation process, and photocatalysis are a few of the technologies that have been recommended and analyzed to remove toxic pollutants from water and wastewater. Among these technologies, photocatalysis is considered as a green technology for removing contaminants, because, its mechanism depends on light irradiation to modify toxic pollutants into non-toxic ones. Mainly, photocatalysis involves the transformation of photon energy into chemical energy. Here, the

photocatalyst plays a major part in developing a transient state by using light absorption (photon energy) and releasing the electron-hole pair producing the chemicals (chemical energy) in the form of the product. Semiconductor photocatalyst significantly plays an important role in the degradation of organic and inorganic pollutants. Due to versatility, ease to synthesis, good controllability, and stability TiO_2 is used for the degradation of many pollutants. The main disadvantage of using TiO_2 which is only acquired in the UV region, which employs <5% of solar light. Due to these drawbacks, various researchers have focused on developing different TiO_2 structures and their nanocomposites, which support the degradation of toxic pollutants in water and wastewater [11].

1.10. Types of Photocatalysts

Based on the phase of the catalyst, photocatalysis was categorized into two types homogeneous and heterogeneous photocatalyst. The catalyst which was in a different phase from the reactants is called heterogeneous catalysis. Transition metal oxides and semiconductors have distinct properties and are the most frequent heterogeneous photocatalysts. It was the most commonly used technique for treating photocatalytic water because it is simple to separate the catalyst material after usage. The decomposition of Rhodamine B dye by silver phosphate nanoparticles under the effect of visible light is an example of heterogeneous photocatalysis. The separation of the used catalyst is a very difficult task in the case of homogeneous photocatalysis. Homogeneous photocatalysis occurs when the photocatalyst and reaction medium is in the same phase. For example, homogeneous photocatalysis is used in the photo-assisted degradation of aqueous organic dye using water-soluble carbon dots [12].

1.11. Working of photocatalyst

A photocatalyst is a natural substance that absorbs light to increase its energy level and then transfers that energy to a reactant to create a chemical reaction. Some of the types of photocatalysts are TiO_2, ZnO, MgO, WO_3, Fe_2O_3, SiC, GaAs, ZnS, GaP, and CdS. Due to its efficient photoactivity, high stability, low cost, and safety to the environment and humans, large stability to light illumination, and nontoxicity, titanium dioxide is majorly used. TiO_2, has a high band gap energy of around 3.2 eV its absorption of solar radiation is bounded to the UV light range, which accounts for only 5% of the solar spectrum. Several studies have concluded that the indirect process predominates over the direct mechanism and makes a major

contribution more to dye degradation than the visible-light-induced process. It is considered that the latter method has a much slower reaction than the indirect method [13].

1.12. Mechanism of Photocatalysis

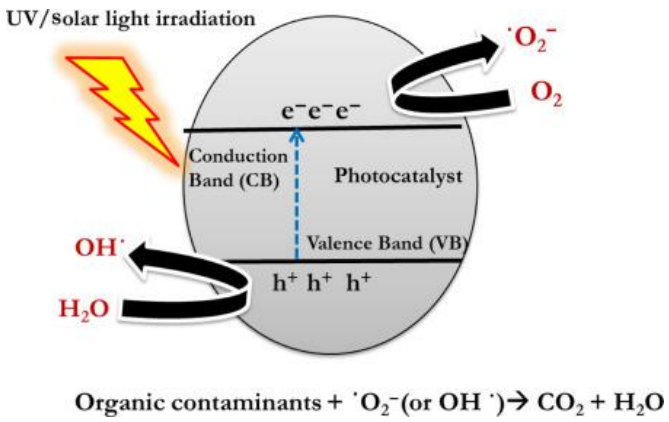

Fig. 1.5 Schematic representation of semiconductor photocatalytic mechanism

Photocatalysis is the activity happens when a light source interacts with the surface of semiconductor materials called photocatalyst. The reaction generally depends on the light (photon) intensity and the catalyst. When lightning reaches the surface of the catalyst the light energy from the light source (UV or solar) excites an electron from the valence band of the photocatalyst to the conduction band, which gives a hole (electron deficiency) in the valence band as well as forms hydroxyl radicals. Due to hydroxyl radicals having the greatest oxidation potential, they can oxidize most organic contaminants. It can be described as

$$TiO_2 + h\nu = e^{-cb}(TiO_2) + h^{+vb}(TiO_2)$$

where cb is the Conduction Band and vb is the Valence Band. The holes would exist in the catalyst's valence band. These holes in the valence band can oxidize donor molecules and interface with water molecules to create hydroxyl radicals (the hydroxyl radicals have strong oxidizing power responsible for the degradation of pollutants). The electrons from the conduction band react with dissolved oxygen species to release superoxide ions, and these electrons trigger redox reactions [14].

1.13. Applications of photocatalyst

i) Self-cleaning Glass- Doping with nanoparticle photocatalyst assembles the glass hydrophobic and the photocatalyst annihilates the bacteria or other contaminants, hence all the time the glass is clean.

ii) Photocatalytic water splitting- Photocatalysts replaces H_2O with H_2 through the oxidation process with light irradiation. An example of a schematic photocatalyst in the UV range is founded on sodium tantalite ($NaTaO_3$) doped with La and loaded with a cocatalyst nickel oxide.

iii) Solar water disinfection- Purification of water by maintained photocatalyst reaction destroys the bacteria inside the water with an oxidation approach.

iv) Other applications such as degradation of organic dyes, volatile organic compounds, antimicrobial, antibacterial, and antioxidant activities, solar cell applications, hydrogen generation, food packaging and biomedical and medical applications [15].

1.14. Advantages of photocatalyst

i) The possibility to use renewable and pollution-free solar energy, photocatalysis offers a good substitute for the energy-intensive traditional treatment methods (adsorption on activated carbon, ultrafiltration, reverse osmosis, coagulation by chemical agents and ion exchange on synthetic adsorbent resins) [16].

ii) In contrast to standard treatment methods that move contaminants from one phase to another, photocatalyst leads to the manufacturing of high-quality products.

iii) Lots of harmful substances can be destroyed using the photocatalytic method in various wastewater streams.

iv) Photocatalyst requires a mild reaction condition, a quick reaction time, and lesser chemical input.

v) The secondary waste generation is the slightest

vi) It can be employed to the extent of aqueous treatment, hydrogen generation, and solid (soil) treatment [17].

1.15. Objectives

1. To synthesis ZnO and Cobalt doped ZnO by co-precipitation method.
2. To study the effect of annealing temperature on structural and optical characteristics of Cobalt doped ZnO.

CHAPTER II
REVIEW OF LITERATURE

2.1. Introduction:

Metal-doped ZnO is a very favourable material for a variety of applications due to its unique optical, electrical, and magnetic properties. ZnO has a wide band gap and high electron mobility, which makes it suitable for various optoelectronic applications. Several studies have reported the successful synthesis of metal-doped ZnO and their properties have been investigated. The metal dopants commonly used in ZnO doping include Al, Mn, Co, Ni and Cu. These metal dopants have been shown to significantly modify the properties of ZnO, resulting in improved performance [18].

The photocatalytic activity of Co-doped ZnO is attributed to its improved charge separation and increased surface area, which leads to enhanced light absorption and higher efficiency of the charge transfer. Co-doped ZnO has also been shown to exhibit excellent stability and high reusability in photocatalytic reactions. In environmental waste management systems, a variety of possible photocatalysts based on semiconductor metal oxides, such as TiO_2, ZnO, ZrO_2, V_2O_5, Fe_2O_3, and WO_3 have been used. ZnO's photocatalytic performance is impacted by a variety of factors, including nanomorphologies, manufacturing process, pH, crystallinity, pollutant composition, and irradiation intensity. Due to the inherent optoelectronic properties (valance and conduction band positions), strong oxidizing power and long-term stability, Titania (TiO_2) as a photocatalyst has the potential to be used in environmental remediation. TiO_2 is a common photocatalyst, but due to its low surface area, its activity is significantly reduced.

However, ZnO is not fully utilized as a photocatalyst due to a number of drawbacks. ZnO's large band gap energy prevents photo absorption in the visible light area, resulting in two major drawbacks. Due to the fast recombination of photogenerated charges, the first is low photocatalytic effectiveness. The second drawback is that zinc oxide only works in the UV part of the solar spectrum, which represents only 4% of all solar light. The photocatalytic degradation efficiency was improved by doping non-metals into ZnO in addition to the metal ion [19].

2.2. Reviews on the synthesis of pure and doped Zinc Oxide:

Karanpal Singh *et al* (2023) [20] have synthesized undoped and Cobalt doped zinc oxide nanoparticles (NPs) through the co-precipitation method. A red shift with the change of absorption spectra is observed in Ultra violet (UV) absorption spectra. X-ray diffraction (XRD) results have confirmed the average crystalline size of the obtained powder. The obtained ZnO NPs are in an arrow size distribution (15-20 nm) having wurtzite crystal structure, according to Field emission scanning electron microscopy (FESEM) and High-resolution transmission electron microscopy (HRTEM) investigation. The synthesized ZnO and Co-ZnO NPs have shown high photocatalytic and antimicrobial effectiveness. The finding from this study thus supports the developed system having dual function as an antibacterial and photocatalytic agent for effective environmental remediation.

Rajwali khan *et al* (2022) [21] have successfully assembled ZnO, and ferromagnetic (Gd, Co) materials are co-doped with ZnO and found that their electrical conductivity is strengthened. Further identified the samples morphology, microstructure, and optical characteristics where the host Co is doped with ZnO and it's verified through UV, scanning electron microscopy (SEM), Transmission electron microscopy (TEM), XRD and Energy-dispersive X-ray (EDX). The tetragonal structure of the (Gd, Co) co-doped specimen was measured through XRD. By using TEM, the morphology of the produced nanotubes was not affected by gadolinium, and cobalt was confirmed**.** There are no defect-related absorption peaks are situated at UV-vis spectra. Also, they observed, by increasing the concentration of co-dopant $\varepsilon_{r,}$ ε'' values are decreased with decreasing frequency and also found there is a strong relation between dielectric response and a.c. electrical conductivity. It has resulted, that the charge carriers are increased by substituting Zn ions with Gd and Co. ZnO was co-doped with (Gd, Co) their property shifted from diamagnetic to ferromagnetic which indicates, there is a significant change in the hysteresis loop. These applications are used in spintronic nanotechnology.

Pham Thi Lan Huong *et al* (2022) [22] have used a facile hydrothermal method for the synthesis of high-purity Co^{2+} doped ZnO nanoparticles with an average size of 20-200 nm to obtain the degradation efficiency of 99.7% for direct blue 71 (DB). They have compared the degradation efficiency between ZnO: Co^{2+} and an undoped ZnO sample under visible light, which have explained the excitons recombination between electron-hole pairs produced by

Co^{2+} ions doped in the ZnO lattice. Charge carrier concentration and particle size are responsible for the decrease in optical-absorption edge with an increase in dopant level (1-7 mol%). Interaction between hydroxyl radicals (OH) and organic dye are mainly attributed to the degradation mechanism of DB71. The outcome of this study has helped them to remove the toxic organic dyes in the aquatic environment using Co^{2+}-doped ZnO materials.

Muhammad Adeel *et al* (2021) [23] have used the precipitation method for degradation of methyl orange under visible light irradiation with the use of Co-ZnO as a photocatalyst. They have analyzed that 10% of Co-ZnO was highly efficient for the photodegradation of methyl orange compared to ZnO. They have examined the impacts of experimental parameters such as pH, temperature, catalyst dosage, recycling of catalyst and dye concentration on photocatalytic activity. They have observed that methyl orange dye was totally degraded in 130 minutes. They have used the treatment of degradation data for analyzing the reaction kinetics in accordance with Eley-Rideal mechanism.

Hamdah S. Alanazi *et al* (2021) [24] have prepared Gd and N co-doped NPs using facile wet-chemical co-precipitation method. The light absorption ability is improved by hetero atom dopant for creating a trap state to act as photo induced-electron hole separator. From the UV-Vis-DRS and Photolumiscence (PL) analysis it has confirmed that the foreign ion doping has enhanced the light absorption ability and suppress the charge carrier recombination. Co-doped with ZnO has shown higher photocatalytic degradation efficiency of about 87% and 93% respectively and they have confirmed the excellent stability for recycling process. From this study, they have believed that the heteroatom Co-doped ZnO is a favorable material for photocatalytic degradation. Finally, they have reported that Gd/N/ZnO could be a promising photocatalyst for environmental application.

Mohammed Ahmed Wahba *et al* (2021) [25] have synthesized multi-wall carbon nanotubes (MWCNTs)/Cobalt-doped zinc oxide nanocomposites by sol-gel method. From the analysis of structural and morphological characterization the formation of ZnO hexagonal wurtzite with cabbage-like structure is confirmed. The homogeneous distribution of MWCNTs in powder is powder is confirmed from the surface-surface contact betweem MNCNTs and ZnO particles which is evidenced by TEM, SEM and XRD. The Co-doping decrease the band gap of ZnO is found on the Kubelka-Munk plot by suggesting a promising photocatalytic activity under visible light. The Vibrating Sample Magnetometer (VSM) measurement has confirmed that Co doping have induced a clear transformation from diamagnetic to ferromagnetic characteristics

through Co^{2+}-Vo-Co^{2+} interactions. The nanocomposite displayed the highest sunlight irradiated photocatalytic activity for degradation of Congo red with degradation efficiency of 96% after 125 min.

Cuiyuan chai *et al* (2021) [26] have analyzed the two-dimensional honeycomb structure in Fe, Co, Ni, and Cu doped ZnO monolayer based on density functional theory. Monolayer ZnO (2.257 eV), Fe/ZnO (0.512 eV), Co/ZnO (0 eV), Ni/ZnO (0.401 eV), and Cu/ZnO (1.738 eV) are the obtained band gaps for quasiparticle. They have analyzed the phonon dispersion curve for stability. Also, they have investigated the in-plane and out-plane strain effect for analyzing any variation in electronic and optical properties of Fe, Co, Ni and Cu doped ZnO monolayer. By applying strain, the tunable band structure and optical properties of Fe, Co, Ni and Cu doped ZnO monolayer such as Indirect-direct band gap transition, shrink and enlargement of the band gap can be achieved. In the optoelectronics field, this type of heterojunction is more conductive in accordance with the absorption spectrum.

S. Vinoth *et al* (2021) [27] have used the chemical bath deposition technique to synthesize cobalt-doped ZnO (ZnO: Co). They have kept the thin films under UV light of wavelength 365 nm to examine the UV photo-sensing properties. The prepared samples have hexagonal wurtzite crystal structure which is revealed by XRD analysis. The prepared Co-doped ZnO described the nanowire morphology in FESEM study. By increasing the Co dopant content by 1%, the optical bandgap value is decreased from 3.23 to 2.97 eV is observed in UV-Vis characterization. Due to the presence of oxygen vacancies, the PL spectra showed some defects in the visible region which confirms high photoabsorption property of the sample. They have understood the availability of components and their binding states in the fabricated thin films that have been carried out by the XPS investigation. Finally, they have confirmed that the ZnO: Co samples are potential candidates for optoelectronic devices.

Aswathi K. Sivan *et al* (2021) [28] have synthesized ZnO nanorods by chemical bath growth by varying Co content from 0 to 20 atomic% in the growing solution. They have reported the modification of optoelectronic behavior of ZnO nanorods through transition metal doping. Cathodoluminescence, time-resolved luminescence, transient absorbance spectroscopy and Incident photon-to-current conversion efficiency (IPCE) are used to examine the optoelectronic behavior. The IPCE of ZnO nanorods was enhanced by co-doping atomic%. Co-doping stretches the light absorption of nanorods into the visible region, increases the surface defects, shortens the non-radiative lifetime by leaving the radiative lifetime constant. The growing

concentration of Co undoped ZnO NR's are measured at 1% and 5%, indicating the higher photogenerated current density. At last, they have reported that by functionlize ZnO to overcome its shortcomings in its usability as a photoanode.

Karim Tanji *et al* (2021) [29] have investigated for the simulation of a pilot-scale photocatalytic reactor based on cobalt-doped ZnO films, where the photocatalyst films are initially assessed on a lab scale for the degradation of rhodamine B (RhB) under visible light. ZnO and cobalt-doped ZnO catalyst films are synthesized by means of the spray pyrolysis technique. The lattice parameters of cobalt-doped ZnO films, as well as their bandgap values and structures, have been computed applying the density functional theory (DFT). Box-Behnken Design (BBD) is used to assess the effect of the main operating parameters on the photocatalytic activity that achieved 93% using 10% of cobalt doping ZnO within 120 min. Aspen Plus is used to model and design the photocatalysis process at the pilot scale based on the lab-scale results. From this study, they have reported that cobalt-doped ZnO films could be effectively used for the photodegradation of organic pollutants and offer potential perspectives on their large-scale application for the treatment of real liquid effluents using solar light.

Khulud Habanjar *et al* (2020) [30] have studied the effect of Co-doping on the structure, optical and magnetic properties of ZnO nanoparticles. Pure ZnO and (Sm, Co) co-doped nanoparticles are synthesized by co-precipitation technique. The XRD patterns of all samples have confirmed the formation of wurtzite- type structure of ZnO with the formation of Sm_2O_3 and Co_3O_4 as minor secondary phases with $x \geq 0.005$. The spherical morphology of pure ZnO is transformed to nanorods as the concentration of Sm^{3+} and Co^{2+} increases. UV–vis spectral analysis is used for the calculation of the energy band gap (Eg) by different methods. Energy band gap and Urbach energy are observed to have a reverse trend. Magnetic properties are investigated by the vibrating sample magnetometer. M − H hysteresis analysis has revealed that for small doping, the samples have a ferromagnetic signal combined with diamagnetic contribution. They have observed that the enhancement in ferromagnetism behaviour for $0.01< x < 0.02$ is justified by the formation of Bound Magnetic Polarons (BMPs) as it significantly enhances with the doping of Sm and Co by stabilizing Zn vacancy and other magnetic defects.

Yingming Wang *et al* (2020) [31] have successfully prepared C-doped ZnO particles by the calcination using microwave hydrothermally prepared metal−organic framework-5 (MOF-5)

as the precursor. MOF-5 is turned into C-doped ZnO through calcination at 500 °C, and its cubic shape is well-maintained. X-ray photoelectron spectroscopic studies has confirmed the C-doping in the ZnO. The as-prepared C-doped ZnO has demonstrated a Rhodamine B (RhB) degradation efficiency of 98% in 2 hours under a solar-simulated light irradiation, much higher than that of C-doped ZnO derived from MOF-5 synthesized by the ordinary hydrothermal method. The trapping experiment has revealed that the crucial factors in the RhB removal are photogenerated radicals.

Javaid Akhtar *et al* (2020) [32] have synthesized pure ZnO, Gd and Nd co-doped ZnO nanorods based nanocomposites through simple hydrothermal method. The XRD results has demonstrated that Gd and Nd ions are incorporated into ZnO lattice in the synthesized ZnO based nanocomposites and showed hexagonal wurtzite structure. The SEM and TEM results have shown that nanorods having nanoscale diameter and length are successfully synthesized by hydrothermal method. The UV–visible spectroscopy has verified that the band gap of ZnO is reduced due to incorporation of Gd and Nd into ZnO photocatalyst. Similarly, Gd and Nd incorporation into ZnO is found effective to reduce the recombination of electrons and holes as confirmed by PL spectroscopy. Moreover, the prepared nanocomposites with various atomic ratios are tested for photocatalytic degradation of methylene blue (MB), under visible light irradiation. The highly efficient and optimized 1.5% Nd/ZnO nanocomposite has demonstrated enhanced photocatalytic performance for the degradation of methylene blue compared to pure ZnO and other nanocomposites. Furthermore, the recycling results has shown that the 1.5% Nd/ZnO nanocomposites have displayed good stability and long-term durability. From this study, they have confirmed that the ZnO based nanocomposite could be efficiently used in various energy and environmental applications.

N. Siva Jyothi and K. Ravichandran (2020) [33] have demonstrated the deposition of Cu, Co, Mn and Mo doped zinc oxide thin films onto glass substrates and also have investigated their photocatalytic dye degradation abilities at different pH values of the test dye solution. The effect of point of zero charge on the photocatalytic activity is studied. This study has demonstrated how the pH of the dye solution have played a crucial role on the dye degrading mechanism. The optimum pH for achieving the best dye degrading efficiency is estimated for all the four doped ZnO films for cationic dyes and the procedure for extending this idea to the anionic dyes are also addressed.

I. Ahmad *et al* (2020) [34] have investigated co-doped ZnO nanoparticles with terbium (Tb) and europium (Eu) that are produced rapidly, inexpensively and rapidly through combustion. The insertion of Eu and Tb ions into the idea of ZnO is confirmed by XRD patterns. When compared to pure ZnO, the crystallite size is relatively small. With a suitable doping concentration, it has been observed that doped Eu and Tb ions can enter the ZnO lattice structure. The resulting doped ZnO has ordered hexagonal wurtzite structures, a nearly spherical morphology, a high specific surface area and a high porosity. The presence of a mixture of $Eu^{2+/}Eu^{3+}$ and $Tb^{3+/}Tb^{4+}$ oxidation states as well as a high concentration of surface-chemisorbed oxygen species, according to further investigation using XPS measurements, also contributed to the strong photocatalytic activity. The yield of CH_4 was efficiently increased by Eu and Tb to 4.59 mol, which was 3.4 times greater than that of pure ZnO.

N.S. Satdeve *et al* (2019) [35] have examined the sonochemical synthesis of ZnO and silver ornamented ZnO (9 wt%) using zinc acetate, silver nitrate and sodium carbonate as precursors. Highest purity hexagonal quartzite crystals of ZnO are revealed by XRD examination. Using XRD analysis, the average crystallite sizes of ZnO and Ag-ZnO are calculated to be 17.53 and 18.73 nm, respectively. Under solar light irradiation, the photo catalytic capabilities of ZnO and Ag-ZnO (doped) nanocomposite are investigated for the breakdown of methylene blue (MB) dye in aqueous solution. Under ideal circumstances, a maximum degradation of MB dyes (96.2%) for Ag doped ZnO nanocomposite was prepared by ultrasound assisted method.

Nikhil Chauhan *et al* (2019) [36] have studied that Nitrogen and cobalt-doped rods like mesoporous ZnO nanostructures are synthesized by hydrothermal method. Crystallite size, band gap energy, elemental composition, charge carrier recombination rate, pore size and surface area, as well as the effect of doping on these parameters, are some of the parameters that can be determined using a variety of characterization tools, including XRD, SEM, TEM, UV-vis, PL, and nitrogen adsorption-desorption analyses. Three water contamination models with different chemical make-ups, such as methylene blue, malachite green, and congo red, are utilised to assess the impact of co doping on the adaptive photocatalytic activity of pure ZnO under visible light.

Huifang Liu *et al* (2019) [37] have worked into the synthesis of Silver-zinc oxide nanocomposite (Ag-ZnO nanocomposite), which was done so to improve the photocatalytic degradation of methylene blue. The synthesised Ag nanoparticles had an average size of about 40 nm, while the ZnO nanorods are 2 m long and 200 nm wide. The ZnO rod surface was well

doped with Ag nanoparticles, according to the morphological analysis. Under UV light irradiation, the photocatalytic degradation of methylene blue by the nanocomposite's performance and stability are assessed. According to the overall findings, 6% of Ag nanoparticles degraded more effectively than the other concentrations and bare ZnO. As a result, the use of Ag-ZnO nanocomposite in treating certain conditions can be considered using waste water.

Lijing Zhang *et al* (2019) [38] have researched ZnO has been successfully synthesised via ion exchange and calcination processes has a homogeneous distribution of sulphur ions. S^{4+} and S^{6+} are the major S elements that are doped, as determined by XPS. They came to the conclusion that combining S 3p with ZnO's upper valence band states caused a uniform distribution of S dopants to increase the valence band maximum. S-ZnO had a maximum valance band of 0.37 eV that was greater than ZnO's. The improvement in the light response was primarily caused by this outcome. We also looked into Ag/S-ZnO's photocatalytic capabilities. MO was photocatalytically degraded at the maximum rate in Ag/S-ZnO by adding 10 weight percent Ag. A photocatalytic mechanism has been identified in this article.

Negin Farhadian *et al* (2019) [39] have examined N, S− doped TiO_2 (NST), N, S− doped ZnO (NSZ) and their composite with chitosan (NST/CS, NSZ/CS) are synthesized by sol gel-hydrothermal method. Under the influence of visible light, tetracycline was photocatalytically degraded using these photocatalysts. The photocatalytic breakdown of tetracycline is nearly twice as fast when chitosan and NST are combined. The reusability of as-synthesized NST/CS was evaluated, and it can be used as an efficient catalyst for the degradation of organic chemicals in water and wastewater, notably for the degradation of developing pollutants such pharmaceutical pollutants, due to its high recoverability. The findings of this study point to a potentially useful material for usage by local government agencies and pharmaceutical facilities in the removal of tetracycline from water resources and the treatment of pharmaceutical contaminants

Eswaran Prabakaran and Kriveshini Pillay (2019) [40] have investigated the synthesis of nitrogen-doped zinc oxide nanoparticles with a cabbage like morphology (N-ZnONCBs) by a hydrothermal method. Under UV light and visible light irradiation at various times, the N-ZnONCB catalyst showed improved photodegradation efficiency (98.6% and 96.2%) and kinetic degradation rates of MB ($k = 0.0579\ min^{-1}$ and $k = 0.0585\ min^{-1}$). Additionally, the photodegradation study was assessed using various N-ZnONCB catalyst dosages, starting MB

concentrations and MB solution pH variations (3, 5, 9 and 11) when exposed to UV and visible light. Total Organic Carbon (TOC) tests are used to assess complete mineralization, and liquid chromatography mass spectra (LC-MS) are used to extract the intermediate photocatalytic degradation products. Additionally, this photocatalyst was examined with 2,4-dichlorophenol (2,4-DCP) under varying exposure times to visible light. The photostability and reusability of the N-ZnONCB catalyst are also evaluated, with a percentage degradation rate of MB (93.2%) after 4 cycle trials. These findings unequivocally show that the photocatalytic degradation of MB from wastewater samples can be accomplished using the N-ZnONCB catalyst.

Mohd Faraz *et al* (2018) [41] has investigated the efficiency of samarium-doped ZnO nanoparticles (1%, 3%, and 5%) produced by a gel-combustion as an effective photocatalyst for the degradation of Malachite green (MG) dye. According to the UV-vis spectroscopic investigations, Sm doping improved the ability of the Sm-doped ZnO nanoparticles to absorb visible light and a redshift for the Sm-doped ZnO nanoparticles appeared as compared to ZnO nanoparticles. When used as scavengers in the photocatalysis procedure, tert-butyl alcohol and the disodium salt of ethylenediaminetetraacetic acid showed that hydroxyl radicals (OH) and holes (h+) are the reactive species in charge of the degradation of MG. The Sm-doped ZnO nanoparticle's recycleability for the MG dye degradation is also demonstrated.

Liu Liu *et al* (2018) [42] have investigated ZnO nanofiber's undoped and doped Fe ions are generated using the electrospinning technique to study the impact of transition metal ion doping on ZnO's photocatalytic activity. It was discovered that by enhancing the sintering conditions, ZnO fibre crystallisation was greatly enhanced. According to the findings, Fe-doping significantly increased ZnO's photocatalytic activity due to altered nanofiber shape and a smaller optical bandgap. For a 1.5% Fe-doping percentage, the ZnO nanofibers displayed the best photocatalytic activity, which was attributed to the ZnO matrix's high concentration of dopant ions. ZnO's improved photocatalytic performance may expand the range of its industrial and commercial uses.

Muhammad Arshad *et al* (2018) [43] have investigated through the application of the precipitation-deposition process, tin-doped zinc oxide (Sn-ZnO) nanoparticles are created in a variety of polar and non-polar solvents, including 2-propanol, acetonitrile, n-hexane, and 3-Methyl-1-butanol. In the presence of non-polar solvent, Sn doping was more advantageous. Sn-ZnO NPs that had already been synthesised had considerable photocatalytic activity (PCA),

which was more encouraging for Sn-ZnO than ZnO. The results showed that the effect of solvents (polar and non-polar) on the doping of Sn with ZnO and the activity of Sn-ZnO NPs as photocatalysts varied. Results revealed that solvent (polar and non- polar) have significant effect on crystallinity, morphology and other physico-chemical properties of Sn-doped ZnO nanoparticles. The variable morphology of synthesized Sn-doped ZnO indicates that future studies can be focused on the synthesis of NPs of varying morphologies.

Petronela Pascariu *et al* (2018) [44] have examined Ni, Co codoped ZnO nanoparticles have been synthesized by co-precipitation method. PL spectra studies shows that the shift in near band edge (NBE). XRD data revealed that Ni, Co codoped ZnO nanoparticles presented pure wurtzite phase. Their photocatalytic activity was investigated by the degradation of Rhodamine B (RhB) dye by visible light irradiation and compared with pure ZnO activity. It seems that increasing doping concentrations of Ni, Co leads to a decrease of the photocatalytic efficiency. Further studies will target fine tuning of Ni and Co concentrations around the one with observed maximum activity and integration of the respective powder in a sensing system in order to verify also sensing ability of the material with best photocatalytic activity.

V. Vaiano *et al* (2018) [45] have studied that numerous photocatalysts based on commercial ZnO modified by silver photodeposition are prepared. Ag/ZnO sample's metallic Ag (Ag^0) composition was demonstrated by XRD and XPS, and the ZnO structure was determined. The presence of more silver particles was demonstrated by TEM examination as the Ag level increases. Finally, Ag/ZnO sample reflectance was found using UV-vis, DRS results. This reflectance band was attributed to the metal silver particle surface plasmon resonance (SPR) absorption. Commercial ZnO and Ag/ZnO samples are assessed for their ability to remove phenol when exposed to UV light. The phenol degradation dramatically dropped after this content (i.e. 1.28 wt%), showing that the ideal Ag content was equal to 0.88 wt%. The optimised Ag/ZnO photocatalyst was then used to treat genuine drinking wastewater that contained phenol and after 180 minutes of UV exposure, almost all of the phenol was removed.

H.V.S. Pessoni *et al* (2018) [46] have examined the single phase Zn1-xCoxO ($0 \leq x \leq 0.05$) ceramics synthesised using a pressure-free solid state reaction technique for their dielectric characteristics and impedance spectroscopy tests. These findings demonstrate that the materials have a defect density within the grain due to the use of pressure-free sintering at high temperatures for an extended period of time. It also results from the electronic inhomogeneous conduction mechanism. Controlling the fault density within a grain with an appropriate

sintering technique is an efficient way to manage the massive dielectric characteristics. These findings also show that, as opposed to the Schottky barriers indicated in the IBLC mechanism, controlling the defect density with the presence of oxygen vacancies within the grain is an efficient technique to regulate the colossal dielectric permittivity (CP) characteristics. As a result of this CP behaviour, ZnO can be employed not only as an opto electrical material but also as a promising material for sensing applications.

Dominic B. Potter *et al* (2017) [47] have studied at the fabrication of aluminum/indium/gallium co-doped ZnO (AIZO), indium/gallium co-doped ZnO (IGZO), and aluminum/gallium co-doped ZnO (AGZO) thin films on glass substrates using aerosol assisted chemical vapour deposition (AACVD). Due to the comparatively low level of disorder in the structure, the AGZO film had the lowest resistivity (1.3×10^{-2} cm) and maximum carrier mobility (7.9 cm^2 V^{-1} s^{-1}). Due to In^{3+} large radius, which increased optical absorption and decreased resistivity, this addition caused the most structural disorder. The oxidised dopants are present in each film, according to an XPS study. The film's morphologies are dependent on the dopant, and gallium seemed to promote better grain development. The more pronounced Urbach tails in the Tauc plots for the IGZO and AIZO films are confirmated. Due to its superior transport capabilities and high quality crystallinity and shape, the AGZO film was the most conductive.

S. Narasimman *et al* (2018) [48] have investigated that a fiber optic magnetic field sensor is proposed and experimentally demonstrated. Pristine and Co doped ZnO nanorods of different Co concentrations (5, 10, 15 and 20 at%) are synthesized using a hydrothermal method. The wurtzite ZnO lattice's Co ions are successfully absorbed into the Zn site without changing the structure, according to XRD and XPS studies. Due to the magneto-optic effect, the changed cladding is correspondingly sensitive to the surrounding magnetic field. The sensor's operational magnetic field ranges in experimental results, is 17.2 mT to 180.8 mT and it has a maximum sensitivity of 18% for Co doped ZnO nanorods (x = 0.15), which exhibit greater magnetization levels.

Refka Mimouni *et al* (2017) [49] have examined that water purification from Methylene Blue using the photocatalytic performance of (Cr,In) codoped ZnO sprayed thin films under sunlight irradiation. The samples crystallised in the wurtzite ZnO phase, according to XRD examination, with a favoured orientation of crystallites towards the (002) direction parallel to the c-axis. The obtained Atomic force microscopy (AFM) and SEM micrographs demonstrated how codoping

increased the roughness of ZnO films. Visible emission indicating the existence of defects plays a crucial role in photocatalysis because surface redox reactions occur on the surface of defects. Therefore, they function as (Cr,In) codoped ZnO photocatalyst active sites. Thin films of (Cr,In) codoped ZnO shown good photodegradation efficiency when exposed to sunshine and continue to operate well even after three reuse cycles.

Heri Sutanto *et al* (2017) [50] have worked on Co thin films coated onto amorphous glass substrates by sol–gel spray coating technique. This doping also narrows the optical band gap and transparency. Band gap (Eg) for undoped ZnO and ZnO: Co with 10 mol% of doping concentration respectively, fell significantly from 3.20 eV to 3.00 eV. The maximum photocatalytic activity in this investigation was found in ZnO with 4 mol% of Co, which degraded methylene blue (MB) by roughly 76.31% for two hours while exposed to UV light. With an increase in Co concentration, thin film's optical band gaps shrank to 3.02 eV and 3.00 eV for undoped ZnO and ZC10, respectively. The most effective sample for the photocatalytic breakdown of MB when exposed to UV light is ZC4.

Gaopeng Dai *et al* (2017) [51] have prepared ordered macro/mesoporous SnS_2/TiO_2 using tetrabutyl titanate as the titanium precursor and $SnCl_4.5H_2O$ as the tin precursor through the template-free aqueous technique. They have tested the photocatalytic activity of SnS_2/TiO_2 by the degradation of composites, and methyl orange(MO) aqueous solution in the presence of simulated sunlight. The SnS_2/TiO_2 composite has a degrading efficiency of 90.9% within 50 min and has shown greater photocatalytic activity with an estimated rate constant of 0.55 min^{-1}. The ordered porous structure can improve mass transfer and light capture where as heterostructure reduces the recombination rate of photogenerated e^- and hole. The ordered macro/mesoporous structure and SnS_2/TiO_2 heterostructure are considered to play synergistic effects in its enhanced photocatalytic performance.

P. Sivakarthik *et al* (2017) [52] have applied a novel one-step microwave irradiation method for the synthesis of high-performance pure and Co and Ni-doped ZnO nanoparticles. With XRD analysis both pure and doped ZnO are hexagonal wurtzite structures and the average crystalline size is about 38, 31, and 22nm are good agreement with TEM. While doping metal ions into the ZnO host lattice they have observed there is a decrease in optical band gap (E_g) and an increase in the rate of surface recombination are indicated through UV-Vis transmission spectra. The degradation reaction of crystal violet(CV) and Methylene Blue (MB) under UV light irradiation are used to study the photocatalytic activity of the nanoparticles. They are

observed that compared to Ni-ZnO and ZnO, the Co-ZnO has a better photocatalytic performance for the degradation of MB. Finally, they have summarized that the resulting materials can be used for photocatalytic destruction of organic pollutants present in wastewater.

Shashi B. Rana *et al* (2017) [53] have used the wet precipitation method for the synthesized pure and Co-doped ZnO nanoparticles. They have confirmed the presence of Co^{2+} ions into the lattice site of Zn^{2+} ions in the host ZnO matrix from XRD analysis. By using the SEM technique, they have confirmed formation of fine and clear spherical nanocrystallite with clear and distinutive boundaries. The elemental composition of Co^{2+} ions effectively in the lattice site of Zn^{2+}, ions are confirmed by EDS spectroscopy. The existence of donor defects and oxygen vacancies in the doped samples is proved by PL and Raman spectra. The blue shift wavelength for a cobalt-doped sample as compared with pure ZnO nanoparticles is displayed in the UV-absorption spectrum. At room temperature, the pure ZnO shows diamagnetic nature whereas Co-doped samples expose ferromagnetic properties. They have used the agar well diffusion technique to analyze the antibacterial properties of the cobalt-doped zinc oxide are further studied against 3 gram negative pathogens and further it is investigated, to have an antibacterial agent to control bacterial growth.

P. Dhatshanamurthi and M. Shanthi (2016) [54] have synthesized Li-doped Ag-ZnO by sonochemically assisted precipitation-decomposition method. The PL spectra has revealed the reduction of recombination of the photogenerated electron-hole pairs, 'Ag' and Li^{+} have traped the photo-excited electrons so the recombination rate decreases. Li-Ag-ZnO is more effective than Ag-ZnO, Li-ZnO, bare ZnO and commercial ZnO for degradation of RO 4 degradation under solar light for effective dye removal, it has been observed that a PH of 7 and a catalyst dosage of 3 gL^{-1} are preferred. They have used COD measurements for the confirmation of the mineralization of RO 4 molecule. The process involving electron trapping by Ag and Li is proposed to have higher photocatalytic activity. They reported that the catalyst they prepared is reusuable.

Yansong Zhou *et al* (2016) [55] have adjusted the space charge layer thickness for the GZNO photocatalyst by using La dopant as an effective modifier. Enhanced water-splitting photocatalytic activity is achieved after La doping. Without using co-catalyst, the quantum efficiency for photocatalytic water oxidation is up to 14.5% for La-doped GZNO at 350 nm. The increased photocatalytic performance is mainly due to the enlarged thickness of the space charge layers and played a major role in the separation of photogenerated charge carriers. They

have adjusted the width of the space charge layers for water-splitting which has resulted in new guidelines for the development of highly effective photocatalysts.

Surya Veerendra Prabhakar Vattikuti *et al* (2016) [56] have used $ZrO(NO_3)_2$ or $(NH_4)_6Mo_7O_{24}.4H_2O$ and C_8H_6S as a precursor to obtain material by wet chemical method. The prepared material is characterized under different methods. The increased photocatalytic activity for methyl orange degradation identified in MZr-2 hybrid samples is about 8.45 times greater than that of pure ZrO_2. They have recycling the experiments have revealed the reusability of hybrid due to their low photocorrosive effect and good catalytic stability. In accordance with the Langmuir-Hinshelwood model, the MZr-2 photocatalyst has followed pseudo-first-order kinetics for the degradation of MO. They have reported that ZrO_2/MoS_2 hybrid photocatalyst can be recollected, filtered during recycling and they have remained still highly active.

Chunxiao Lu *et al* (2016) [57] have prepared an up-conversion luminescence agent (Er^{3+}: $YAlO_3$) which can effectively transform the visible light in solar light into ultraviolet light. The crystal forms, particle sizes, chemical compositions and weight change process of Er^{3+}: $YAlO_3$/Fe and Co-doped Tio_2–ZnO coated composites are analyzed. The photocatalytic activities of the composites are evaluated through the degradation of azo fuchsine under visible light irradiation. It indicated that the visible light photocatalytic reduction ration of Fe and Co doped TiO_2–ZnO composites are 47.8 and 67.9 %, while after adding 15 wt% Er^{3+}: $YAlO_3$, the reduction ratio reached 93.5 and 95.5 % respectively. They resulted the photocatalytic effect Er^{3+}: $YAlO_3$/Co-doped TiO_2 is better than that of Er^{3+}: $YAlO_3$/Fe-doped TiO_2-ZnO.

A.S. Manikandan *et al* (2016) [58] have applied a microwave assist process for the synthesis of undoped and Co-doped ZnO powders. The synthesized powders have shown two types of nanoparticles disc-shaped and needle-shaped which has the strongest ferromagnetism in comparison with spherical shaped Mg doped ZnO. The diamagnetic activity of undoped ZnO with a hexagonal rod shape was studied in surface morphology. The presence of expected elements Zn, O, Co and Mg was explained by EDAX. The enhanced antibacterial activities against gram-negative bacteria including E-coli and Vibrio cholera is observed for both the doped ZnO nanopowders compared with the undoped ZnO nanopowders. They have reported that between Co and Mg-doped ZnO nanopowders, the former is superior in photocatalytic and bacterial activity.

Rimzhim Gupta *et al* (2016) [59] have achieved Co-doping of a transition metal ion (Cu) and non-metal ion (N) on metal oxide substrate ZnO for the first time. The transition metal doping and N doping is carried out using combustion synthesis and a hydrothermal method, respectively. The combined effect of Cu and N doping is observed by varying the Cu percentage and keeping the nitrogen doping percentage constant. The catalysts are characterized by a wide variety of techniques. Incorporation of Cu and N in the ZnO matrix have introduced sub energy bands near the conduction band and valence band, respectively and facilitates the absorption of longer wavelength spectra. These sub energy levels have also acted as trapping sites for excitons. This results in reduced recombination and enhanced photocatalytic activity is confirmed by PL. The photocatalytic inactivation of Gram-negative bacteria (E. coli) is investigated using the N and Cu co-doped ZnO under UV and visible irradiation with different atom% of Cu. Kinetic analysis is used to obtain the order and rate constant of the inactivation reactions.

Ahmad S. Alshammarai *et al* (2015) [60] have prepared C-doped ZnO with a large surface area through F127-assisted pyrolysis at 500˚C and have used for visible-light-responsive photocatalytic water purification. The band structure of the C-doped ZnO is investigated using valance band XPS and DFT simulation. The C-doped ZnO has possessed enhanced absorption of UV and visible light, though it has showed lower visible-light-responsive photocatalytic activity than ZnO because of significant recombination of photogenerated charge carriers arising from overloaded C-dopant and oxygen vacancies.

J. El Ghoul *et al* (2015) [61] have reported the synthesis of $Zn_{1-x}Co_xO$ nanoparticles prepared by a sol–gel processing technique. The structural properties have shown that the obtained nanoparticles are single phase wurtzite structure and no secondary phases are detected which indicated that Co ions substituted for Zn ions. The energy gap has decreased gradually with increasing doping concentration of Co. The PL spectra has shown a shift of the position of the ultraviolet emission to long wavelength and the intensity decreases with increasing Co. The Magnetic measurements at room temperature reveal diamagnetic behavior for sample with lower concentration and the presence of both paramagnetic and ferromagnetic behavior for increasing concentration.

Christian Fettkenhauer *et al* (2015) [62] have carried out a simple one-step procedure for the preparation of cobalt oxide–carbon nitride composites. From this method, they are able to control the structure of the polymer constituent by the proper selection of the second eutectic

component. With respect to this alkali metal chlorides and zinc chloride have given rise to poly (triazine imides), while tin (II) chloride delivers melon-based polymers. The crystallinity of the carbon nitride polymer phase is influenced by varying the concentration of the precursor in the melt. Cobalt oxide loading in the final products is increased by decreasing the precursor concentration in the melt. The products are highly active photocatalysts for Rhodamine B degradation as exemplified by SnCl2/CoCl2-derived solids, and the water oxidation reaction (WOR). The activity of the products in the WOR is comparable with that of the bench composite photocatalyst prepared by using the three-step procedure that includes the synthesis of Co3O4 nanoparticles as a separate step, thus illustrating the advantages of the developed salt melt assisted approach.

J.J.Maciasi-Sanchez *et al* (2015) [63] have synthesized nitrogen-doped ZnO material by the sol–gel method using zinc acetate as the precursor and urea as the nitrogen source. Bare ZnO is also prepared for comparison. The influence of N doping on structural, morphological, optical and photocatalytic properties is investigated. The photocatalytic activity of N-doped ZnO catalysts is evaluated during the degradation of a mixture of herbicides under visible radiation ≥400 nm. The photo-absorption wavelength range of the N-doped ZnO samples is shifted to longer wavelength and is compared to those of the unmodified ZnO. Among different amounts of dopant agent, the 30% N-doped ZnO material has shown higher visible- light activity is compared with pure ZnO. Several degradation by-products are identified by using HPLC and ESI-MS/MS. The enhancement of visible photocatalytic activity of the N- doped ZnO semiconductor could be mainly due to their capability in reducing the electron–hole pair recombination.

Eric Selorm Agorku *et al* (2015) [64] have synthesized Co-doped graphene–ZnS nanocomposite using co-precipitation method. From UV/Vis diffuse reflectance spectroscopic analysis bandgap energies are estimated. They have chosen the laboratory experiments with indigo carmine (IC) dye as a model for organic pollutants and is used to evaluate the photocatalytic performance of Co-doped ZnS–rGO nanocomposite under visible light. The Co-doped ZnS–rGO has shown significant visible light induced photocatalytic activity towards the degradation of IC. The highest photocatalytic activity for the 0.3 % Co-doped ZnS–rGO sample is observed whereas the bare ZnS showed the lowest photodegradation efficiency. The results have shown that the control of Co doping in the nanocomposite is very important to prevent electron–hole recombination. Finally, they have concluded that the synergistic effect of rGO

and Co in the nanocomposites have led to enhanced utilization of solar energy in photodegradation of IC dye through narrowing of band gaps.

Vijayaprasath Gandhi *et al* (2014) [65] have synthesized $Zn_{1-x}Co_xO$ nanoparticles by a coprecipitation method. It is founded that the crystalline sizes of synthesized samples decrease with the increase of cobalt content from the X-ray diffraction calculation. The FT-IR spectra have confirmed the Zn−O stretching bands at 468, 456, 452, and 461 cm−1 for the respective ZnO NPs. SEM images have demonstrated the distinct flowerlike morphology. The photoluminescence spectra of all the samples have exhibited a broad emission in the visible range. The carriers (donors) bound on the Co sites is observed from the micro-Raman spectroscopic studies. The pure and Co-doped ZnO NPs has shown significant changes in the M−H loop where the diamagnetic behavior of ZnO changes to ferromagnetic nature when doping with Co. They have concluded that the oxygen vacancies and zinc interstitials are found to be the main reasons for room-temperature ferromagnetism in the Co-doped ZnO NPs with the support of the results obtained from the EPR, photoluminescence, and micro- Raman studies.

C.Y. Wang *et al* (2014) [66] have prepared Mg–Al co-doped ZnO thin films through radio-frequency reactive magnetron sputtering technique. X-ray diffraction investigation has shown all the thin films with different Mg: Al ratio have hexagonal wurtzite structure. All the thin films prepared have shown preferential orientation of ZnO. It is observed that when Al concentration is kept constant but Mg concentration is increased, the grain size has decreased at first and then it has increased. UV–vis spectra have shown the thin films have a high average transmittance of 80% in the visible range. PL showed all the thin films had four main peaks located at 386, 410, 463, and 499 nm. The origin of blue peak is oxygen vacancy. When Mg concentration was kept constant but Al concentration was increased, I–V curve presented that for both of the heterojunctions the rectifying behavior was formed. It is confirmed that the conductivity of Mg: Al1⁄41:1 thin film is higher than that of Mg: Al1⁄41:0 thin film. It is found that after illumination, light I–V curve has deviated from rectifying character.

Giwoong Nam *et al* (2014) [67] have investigated the structural and optical properties of Co-doped ZnO thin films have been prepared by a sol–gel dip-coating method. The X-ray diffraction analysis has shown that the thin films has been grown with a c-axis preferred orientation. The position of the (002) peak is almost the same in all samples, irrespective of the Co concentration. It is thus clear that Co doping had little effect on the position of the (002)

peak. For confirmation, the Co^{2+} is substituted for Zn^{2+} in the wurtzite structure, optical measurements are conducted at room temperature using UV-visible spectrometer. It is observed that three absorption peaks are apparent in the Co-doped ZnO thin films that do not appear for the undoped ZnO thin film. They have founded that, as the Co concentration is increased, absorption related to characteristic Co2+ transitions have increased because three absorption band intensities and the area underneath the absorption wells between 500 and 700 nm have increased with increasing Co concentration. It is confirmed that the optical band gap and static dielectric constant is decreased and the Urbach energy and extinction coefficient is increased with increasing Co concentration.

Amalia Mesaros *et al* (2014) [68] have synthesized Co: ZnO nanoparticles by an alternative wet-chemical synthesis route using the SimAdd technique. The obtained samples are investigated by FT-IR spectroscopy, X-ray diffraction and thermal analysis correlated with evolved gas analysis for determining their chemical nature, crystalline structure and for establishing the decomposition sequences. The precipitates prepared are generally amorphous, but low-intensity reflection peaks assigned both to the zinc oxalate dihydrate, and zinc hydroxide have been observed in the recorded patterns, indicating that hydroxy-oxalate precipitates are obtained. XRD studies has revealed a hexagonal wurtzite-type structure for all Co: ZnO samples. TEM investigations have shown particle size between 28 and 37 nm, with spherical and polyhedral shapes and with tendency to form aggregates. The ferromagnetic behaviour of the samples is revealed. From this study, they have reported that by varying the cobalt concentration it is possible to modulate the structural, morphological, optical and magnetic properties.

Michele Karoline Lima *et al* (2014) [69] have synthesized pure and Co-doped ZnO nanoparticles with different cobalt levels through adapted sol–gel method. The results have shown that all the samples have hexagonal wurtzite structure, with no evidence of any secondary phases until 10 mol% of the dopant. The average crystallite size of the samples is in the range of 25–50 nm, do not showing significant differences with the increase of the dopant level. However, the band gap energy of the nanoparticles has decreases from 2.98 eV (pure ZnO) to 1.95 eV (10 mol% of Co). The photocatalytic activity of the samples is evaluated on the removal of methylene blue under visible light irradiation, which has revealed an efficiency reduction by Co-doping ZnO. They have also carried out the antibacterial property indicating activity of the prepared samples against gram-positive bacteria.

G. Poongodi *et al* (2014) [70] have studied Pure and S doped ZnO thin films have been synthesized by hydrothermal method at 90°C for 3h. Studies on the transmission of UV and visible light revealed that S doping decreased the optical band gap of ZnO. Under visible light illumination, the effect of S doping on the photocatalytic activity of ZnO thin films for the degradation of methylene blue dye was investigated. The findings indicated that S doping causes considerable MB degradation. As a result, the S doped ZnO thin films can effectively block UV light while also having improved photocatalytic and antibacterial properties. The vertically aligned ZnO rods have a diameter of roughly 200 nm, according to FE-SEM pictures. S doped ZnO thin films have been found to have increased photocatalytic and antibacterial activities when Reactive oxygen species (ROS) is produced.

Sini Kuriakose *et al* (2014) [71] have examined that Cobalt doped ZnO nanodisks and nanorods are synthesized by a facile wet chemical method. For sunlight-driven degradation of an aqueous methylene blue (MB) solution, the photocatalytic activities are assessed. In comparison to pure ZnO nanodisks and nanorods, the results demonstrated that Co doped ZnO nanodisks and nanorods exhibit significantly increased photocatalytic activity. Due to the increased surface area and high crystallinity of nanodisk structures, both ZnO and Co doped ZnO nanostructures demonstrated higher photocatalytic efficacy towards degradation of MB dye under sunlight irradiation. They have shown that an increase in the photocatalytic activity of ZnO nanodisks and nanorods results from a greater surface area and ideal Co doping. Co doping makes it easier for photogenerated charge carriers to be separated from one another in ZnO, which prevents their recombination. Additionally, a greater surface area aids in improved dye adsorption for effective dye degradation.

Shibin Sun *et al* (2013) [72] have explored that ZnO nanoparticles with diameters of 20–50 nm are initially prepared by solvothermal route using ZnCl2 and ethylene glycol as raw materials. A quick, effective and green vacuum atmosphere approach is used to synthesise N-doped ZnO nanoparticles using the as-prepared ZnO nanoparticles as the precursor and melamine as the N source. In comparison to the undoped ZnO nanoparticles, the N-doped ZnO nanoparticles showed noticeably better photocatalytic performance for the breakdown of methyl orange under simulated daylight irradiation. The increased crystallinity of the N-doped ZnO nanoparticles and the expansion of light absorption towards the visible-light band both contribute to the enhanced photocatalytic performance.

LI Xue *et al* (2013) [73] have explored that Co-doped ZnO nanorods are prepared by electrochemical deposition method in aqueous solution. The samples exhibit a rod-like structure with hexagonal cross sections and a roughened surface, as shown by the SEM photographs. Because Co^{2+} ions penetrated the ZnO lattice, the (002) diffraction peak of Co-doped ZnO nanorods in XRD has a minor shift. At room temperature, PL spectra of the samples are detected. The UV emission of the co- doped ZnO exhibits a minor red shift in comparison to that of the undoped ZnO. As a result, they can conclude that the Zn^{2+} ions in the ZnO samples have been replaced by Co^{2+} ions. The photocatalysis capabilities of co-doped ZnO nanorods are studied under the irradiation of visible light. Additionally, co-doped ZnO nanorods made via electrodeposition as a photocatalyst have significant practical use.

R. Siddheswaran *et al* (2013) [74] have investigated that Pure and Co, Al co-doped ZnO ($Zn_{1-x-y}Co_xAl_yO$; x = 0.04, 0.03, 0.02; y = 0.01, 0.02, 0.03) nanoparticles are synthesized by wet chemical combustion method at 500°C for various doping levels using zinc, cobalt and aluminium nitrates as precursors. Structure, shape, and the presence of magnetism in sintered and combusted pure and doped ZnO materials are investigated. Both the sintered compacts of pure ZnO and the calcined nanoparticles displayed paramagnetism at room temperature. The calcined particles have a size of around 25 nm, and calcination reduced their flaws and cluster nature. Pure ZnO that has been calcined and sintered exhibits a diamagnetic behaviour. The ferro magnetism at room temperature is visible in the Co, Al co-doped ZnO nano powders that are calcined at 600°C, and it rises with Co concentration.

Yan-Gu Lin *et al* (2012) [75] have explored that C-doped ZnO hierarchically porous nanoarchitectures are synthesized in situ on indium tin oxide (ITO) through a counter strategy. For the first time, a comprehensive evaluation of the Polyelectrochemical (PEC) performance of C-doped ZnO nanoarchitectures in water splitting without sacrificial reagents was conducted. They not only have a maximum incident-photon-to-current-conversion efficiency (IPCE) value of 95%, but they also have an IPCE at the monochromatic wavelength of 400 nm as high as 26.6%. This suggests that the modification caused by carbon doping significantly increases the light utilisation and conversion efficiency in the targeted visible region compared to results obtained using a conventional ZnO structure.

Hongchao Ma *et al* (2012) [76] have reported that the preparation of Cu-doped Zn/ZnO composites with carbon modification via simple replacement–hydrothermal method using Zn

powder and CuSO4.5H2O as raw materials. The findings demonstrated that Cu doping increases optical absorption in the visible region, limits phase transfer of metallic Zn to ZnO, inhibits photogenerated electron and hole recombination and promotes ZnO crystal formation. It's interesting to note that carbon attached to the composite surface was created from CO_2 dissolved in solution (supported by XPS data). The degradation of the anthraquinone dye (reactive brilliant blue KN-R) in solution under sunlight irradiation was used to gauge the photocatalytic effectiveness of the catalysts as they are synthesised. The Cu-doped Zn/ZnO composite was successfully prepared under ideal conditions of 2.0 at% hydrothermal treatment at 180 C for 2 h. The preparation of various metal ion-doped metal oxides using this synthetic method may open up possibilities for improving photocatalysis.

Muhammad Ahsan Shafique *et al* (2012) [77] have investigated whether cobalt doping affects the structural, absorbance and magnetic characteristics of ZnO nanoparticles. Co-precipitation was used to create cobalt-doped ZnO in three different compositions ($Zn_{0.99}Co_{0.1}O$, $Zn_{0.97}Co_{0.3}O$, and $Zn_{0.95}Co_{0.5}O$). Although greater doping ratios indicated the presence of extra phases, XRD revealed the typical ZnO wurtzite crystal structure without any lattice distortion caused by impurities. At lower doping ratios but with the inclusion of new phases at greater doping, FTIR also supported the conventional ZnO profiles. VSMR at ambient temperature revealed soft ferromagnetic behaviour for low impurity samples and stronger ferromagnetic behaviour for increasing doping. The temperature of the precursors decomposition was discovered by DSC/TGA investigation in order to fabricate Co-doped ZnO.

Yabo Wang *et al* (2012) [78] have examined that Cobalt based phosphate catalysts (Co−Pi) are loaded on the surface of ZnO by photochemical deposition in a neutral phosphate buffer solution containing Co_{2+} ions. The amorphous Co-Pi phase that was created was uniformly deposited as a coating of nanoparticles on the surface of ZnO. The photocatalytic oxidation of water over Co-Pi loaded ZnO directly revealed the increased activity for oxygen evolution. The amount of oxygen created in the first hour was more than 4 times what would have been possible with just ZnO. The findings imply that CoPi served as a cocatalyst, able to trap photogenerated holes and increase the effectiveness of electron and whole separation. In both systems, photocorrosion of ZnO was also noted.

Rongliang He *et al* (2012) [79] have been investigated on Co-doped ZnO nano powders the location of dopant ions and the effect of doping level on the photo-catalytic activity. Co-precipitation was utilised to create ZnO nanoparticles with a diameter of 50 nm or less that are

doped with up to 5% Co. The findings demonstrated that the Co ions in the ZnO crystal lattice replaced the Zn ions and caused lattice shrinkage. TEM analysis and synchrotron X-ray diffraction are combined with X-ray absorption spectra to demonstrate that Co atoms successfully replaced Zn atoms in the ZnO lattice. It has been shown that Co doping can successfully reduce ZnO's photocatalytic activity and that changing the Co-doping level can affect how quickly photostyrene degrades. The photoactivity was only loared by 1% of the original amount, to 18%.

B. Subash *et al* (2012) [80] have explored that the synthesis of Ce co-doped Ag–ZnO (Ce–Ag–ZnO) by a solvothermal method. For the breakdown of Napthol Blue Black (NBB) dye in aqueous solution under solar light irradiation, the photocatalytic activity of Ce-Ag-ZnO was examined. Co-dopants cause ZnO's absorbance to shift to the visible spectrum. For the mineralization of NBB dye under solar light irradiation, Ce-Ag-ZnO is found to be more effective than Ag-ZnO, Ce-ZnO, commercial ZnO, produced ZnO, TiO2-P25, and TiO2 at pH 9. By measuring COD, it has been demonstrated that NBB dye has mineralized. The visible regions absorption was higher due to the decreased reflectance. The enhanced photocatalytic activity of the catalyst is explained by a mechanism involving the trapping of electrons by Ag and Ce.

Li Liu *et al* (2011) [81] have investigated the electrospinning method for producing pure and co-doped (0.3 wt%, 0.5 wt%, and 1 wt%) ZnO nanofibers, which are then subjected to calcination at 360°C, co-doped nanofibers have better acetone sensing characteristics than pure ZnO nanofibers. As compared to pure nanofibers (approximately 4.4), 0.5 wt% Co-doped ZnO nanofibers respond to 100 ppm acetone at a response of about 16, which is 3.5 times higher. In particular, even in a mixed gas environment, Co-doped ZnO nanofibers can successfully discriminate between acetone and ethanol/methanol. The combination of these nanofibers 1D nanostructure and the Co-doping effect accounts for their high response and speedy reaction/recovery. The outcomes show the possible use of Co doped ZnO nanofibers for producing very effective acetone sensors.

Mohd Arshad *et al* (2011) [82] have explored the sol-gel process used for synthesis Co doped ZnO nanoparticles. All samples formed a single phase, as demonstrated by XRD examination, which was further verified by FTIR data. Crystallite size was seen to change from 27.1 to 21.3 nm as Co concentration increased from 0% to 5%. It implies that Co doping in ZnO can be used to stop crystal formation. It was discovered that the optical band gap increased somewhat as

the Co content increased, confirming the size decrease brought on by Co doping. The presence of Co doped samples is confirmed by EDAX spectra. Based on the Tauc relation, the band gap of the doped samples exhibits a broadening effect. The optical and structural characteristics of ZnO nanoparticles can thus be controlled by cobalt doping.

Manjula G. Nair *et al* (2011) [83] have examined that the structural, optical, photo catalytic and antimicrobial properties of pure and cobalt doped ZnO nanoparticles synthesized by Co-precipitation method. These samples XRD characterization revealed that wurtzite ZnO-structured phase pure nanoparticles had formed. The absorbance spectrum shifted towards the blue with increasing doping concentration, according to optical tests. The produced nanoparticles have a seed-like shape and breakdown Methylene Blue (MB) in the UV region when pure ZnO and ZnO doped with cobalt are synthesised. ZnO can be doped or implanted with appropriate metals at varying concentrations to increase its photocatalytic activity. It is obvious that cobalt doping in ZnO makes ZnO more effective against germs is discussed. The creation of such photo catalysts may be viewed as a milestone in the widespread application of visible light-based heterogeneous photo catalysis to solve water contamination and environmental pollution.

Sousan Rasouli and Shirin Jebeli Moeen (2011) [84] have studied that, cobalt-doped ZnO nanoparticles are synthesized by combustion method. Fuel is made of citric acid and glycine mixtures. According to XRD patterns, varied fuel mixtures caused the development of pure ZnO phase during the combustion event. Reflectance spectra demonstrated that richer green colours can be produced by using greater C/G ratios. Green cobalt-doped ZnO nanocrystalline pigments have been created through combustion in the presence of various glycine and citric acid concentrations. With glycine content, the crystallite size increases from 37 to 63 nm. The fuel ratio affects the shape of synthetic powders. Greater glycine content led to a deeper green colour with respect to greater C*, h and intense green reflection (530 nm).

M. Nirmala and A. Anukaliani (2011) [85] have investigated ZnO nanopowders doped with 5 and 10 at% cobalt are synthesized and their antibacterial activity. Using the DC Thermal Plasma technique, cobalt doped ZnO powders are created. SEM and HRTEM observations of the particle size and morphology revealed a rod-like structure. Gram-negative bacteria Escherichia coli and Gram- positive bacteria Bacillus atrophaeus are subjected to the antibacterial activity of undoped ZnO and cobalt doped ZnO nanoparticles. According to the

antibacterial studies, Co doped ZnO has remarkable antibacterial action, particularly against S. aureus.

Ashokrao B. Patil *et al* (2010) [86] have accomplished that the S-doped ZnO is prepared by new ecofriendly method, which involves simple mechanochemical synthesis followed by thermal decomposition of bisthiourea zinc oxalate (BTZO) powders. The single phase wurtzite structure for S-doped ZnO and the expansion of sulfur lattice constants are suggested by XRD data. PL spectra at room temperature reveal higher oxygen vacancies in S-doped ZnO than in pure ZnO. Using a batch photoreactor, the solar photocatalytic degradation (PCD) of resorcinol was used to test the photocatalytic activity of S-doped ZnO. It was discovered that S-doped ZnO had a PCD efficiency that was two times larger than pure ZnO. They have addressed the fundamental connection between S-doped ZnO photocatalytic activity and PL intensity.

G.G. Nakhate *et al* (2010) [87] have explored that the synthesis of undoped and Ni-doped nanosized TiO2 was carried out at low temperature (at 120°C) using hydrothermal method. The suggested process is simple to scale up and efficient for the synthesis of visible light driven photocatalysts. The nickel was doped with NiO, according to the XRD data. Ni-doped TiO2 samples have spherical shape in SEM images, and hydrothermally treated TiO2 samples have nanofibered particles. The red shift at 550 nm seen by DRS analysis was caused by Ni's absorption by TiO_2. They claimed to have a highly effective catalyst for the visible-light-induced breakdown of MB. They consider that the degradation of dye, organic waste etc. might benefit from our synthetic method for creating visible light photocatalysts by doping the transition metal ions in TiO_2.

Huaming Yang and Sha Nie (2009) [88] have investigated that Co-doped ZnO nanomaterials (CZN) with Co content from 2 mol% to 10 mol% synthesized via a novel freeze-drying route. Without metal cobalt, cobalt oxides, or composites in the samples with Co concentrations below 6 mol%, all samples had a similar hexagonal wurtzite phase. According to a TEM image, CZN (4 mol% Co) is crystallised at a size of 40 nm on average. By comparing the band gap energy of pure ZnO and CZN (2 mol% Co) are 3.11 eV and 2.83 eV. The samples Zn ions are methodically replaced by Co ions, according to the lattice parameters, without affecting the crystal structure. The shape of CZN is spherical with considerable aggregation. Because it is challenging to produce consistent, dependable p-type ZnO, CZN can be beneficial for transparent electrodes in flat-panel displays and metal-insulator-semiconductor (MIS) diodes that could substitute p-n junctions to utilise ZnO's electroluminescence capabilities.

Baiqi Wang *et al* (2009) [89] have studied that Pure and Co-doped ZnO nanorods have been synthesized by a hydrothermal process. The structure and morphology investigations reveal that Co doping can affect the nanorods morphology and marginally hinder ZnO crystallinity, but it cannot alter the preferred growth direction of ZnO nanorods. About 3.0 at% of ZnO nanorods contain Co doping, and dopant Co^{2+} ions replace Zn^{2+} ions at those sites without producing a secondary phase. Co doping has a considerable impact on ZnO nanorod size and shape. Optical experiments show that Co doping can significantly change the energy band structure and increase the amount of defects and oxygen vacancies in ZnO nanorods. These changes are that cause the emission peak of the UV region to shift towards longer wavelengths and the luminescence intensity of the VL region to be noticeably increased.

Igor Djerdj *et al* (2008) [90] have investigated that the structure and the magnetic properties of 3 and 5 mol% (based on the starting concentrations) Co- and Mn-doped ZnO nanorods, synthesized by a simple nonaqueous sol–gel route based on benzyl alcohol as solvent. X-ray spectroscopy, magnetization measurements and electron paramagnetic resonance. The dimensional parameters as well as the degree of aggregation of the doped ZnO nanocrystals as-synthesized retain the wurtzite structure with a morphology in the form of nanorods developed along the [001] direction. The ferromagnetic Co-doped ZnO powders have a Curie temperature above room temperature. The Co^{2+} incorporation in an interstitial site within the Zn O matrix is probably the cause of the obvious increase in the ZnO lattice parameters in comparison to undoped ZnO in the case of Co doping. The observed results thus imply that the manufactured ZnO nanorods magnetic ground state is highly dependent on the type of dopant.

CHAPTER III
MATERIALS AND METHODOLOGY

3.1. Introduction

In determining the particle size, particle size distribution, morphology, and composition there are two basic methods. They are direct and indirect method. Direct method physically examines the particles and measures their dimension while the indirect method focuses on the correlation between particle behaviour and its size. In this chapter, the various characterization techniques such as powdered X-ray diffraction (XRD), UV-visible (UV-vis) spectroscopy, Fourier Transformation Infrared Spectroscopy (FTIR), Photoluminescence (PL), Scanning Electron Microscopy (SEM) are discussed. The information related to particle size, composition, structure, crystal phase and properties of the particles can be determined by an indirect method using spectroscopy-based techniques like UV-vis, XRD, and FTIR. SEM and TEM are the direct methods for identifying the size and morphological characteristics of the particles. An XRD results in a diffraction pattern, which is then compared to the documentation provided in a widely known crystallographic database. With the help of this activity we can determine the size, structure, preferred crystal orientation, and phases that are present in samples. The functional groups absorbed to the surface of the nanoparticles are examined by FTIR spectroscopy. The fundamentals and basic principles of the characterization methods are mainly discussed.

3.2. Chemicals for the synthesis of Pure and Co Doped ZnO particles

- Zinc acetate dihydrate $Zn(CH_3COO)_2.\ 2H_2O$
- Cobalt Acetate $Co(CH_3COO)_2.\ 2H_2O$
- Sodium hydroxide (NaOH)
- Methyl orange (MO) dye

To prepare solutions, distilled water was applied in all steps.

3.3. Physical and Chemical Properties of the Chemicals

3.3.1. Zinc acetate dihydrate

Zinc (2+) is the cationic compound of zinc acetate, which is the chemical formula Zn $(CH_3CO)_2$, most commonly found as the dehydrate Zn $(CH_3CO_2)_2.2H_2O$. It serves as an

astringent. Both the hydrates and anhydrous forms are colourless powders used as dietary supplements.

- Chemical name – Zn $(CH_3COO)_2$. $2H_2O$
- Molecular weight (g/mol) - 219.50 g/mol
- Density - 1.735 g/cm^3
- Appearance - White crystalline solids
- Melting point - 237°C
- Odour - Faint vinegar odour
- Uses - Used for manufacturing polymers, treating zinc deficiencies, dye mordant, and waterproofing agent.

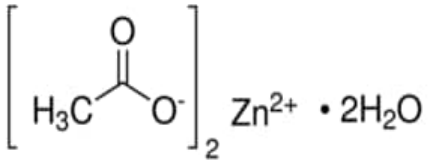

Fig. 3.1 Molecular structure of zinc acetate dehydrate

3.3.2. Sodium Hydroxide

Sodium hydroxide is an ionic compound having the chemical formula NaOH. The hydroxide anion and sodium cation are present. It easily absorbs moisture and carbon dioxide in the air. Their common names include caustic soda and sodium hydrate.

- Chemical name - NaOH
- Molecular weight (g/mol) - 40.0 g/mol
- Density - 2.13 g/cm^3
- Appearance - White crystalline solids
- Melting point - 318.4°C
- Boiling point - 1.388°C
- Odour - Odourless
- Uses - Production of soaps and detergents, textile industry, making glass, water treatment, used in salt spray testing, etc.

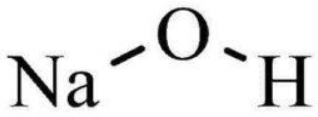

Fig. 3.2 Molecular structure of sodium hydroxide

3.3.3. Cobalt (II) Acetate Tetrahydrate

Cobalt (II) acetate is naturally occur in rocks, soil, water, etc. In small amounts cobalt is an essential element for life, as it is part of vitamin B12. It is used to prepare metal complexes having unusual coordination geometry. Also used as a bleaching agent, drier for coatings and foam stabilizer.

- Chemical name – $(CH_3COO)_2Co.\ 4H_2O$
- Molecular weight - 249.09 g/mol
- Density - 1.71 g/mol[3]
- Appearance - Pink to red powdered granules
- Melting point - 140°C
- Odour – Pungent, vinegar-like odour
- Uses - Used in sympathetic inks, feed additives, catalysts and anodizing, etc.,

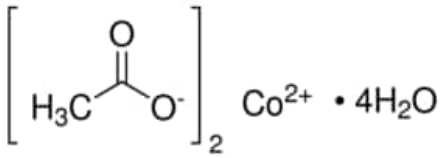

Fig. 3.3 Molecular structure of Cobalt (II) Acetate Tetrahydrate

3.3.4. Methyl Orange

Methyl Orange is an azo dye used as a pH indicator that is commonly in titration due to its distinct and visible colour variation at various pH levels. Methyl orange exhibits a red colour in an acidic medium and a yellow colour in a basic medium.

- Chemical name – $C_{14}H_{14}N_3NaO_3S$
- IUPAC name – Sodium 4-{[4-(dimethylamino)phenyl]}benzene-1-sulfonate
- Molar mass – 327.33 g/mol
- Density - 1.28 g/cm^3
- Appearance – orange or yellow
- Melting point - 300°C
- Uses – indicator for titration, rarely used in textiles applications because of its sensitivity to acids, printing, and dyeing.

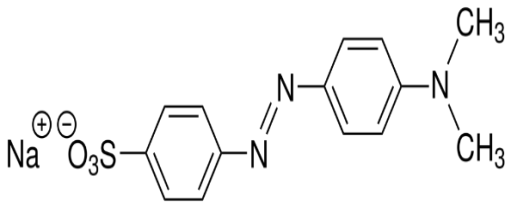

Fig. 3.4 Molecular structure of Methyl Orange

3.4. Co-precipitation method

There are two principles for the preparation of heterogeneous catalysts, the impregnation of preformed supports with a solution of the active metals is known as Co-precipitation, where one or more metals are precipitated together with the support or its precursor. The coprecipitation methods involve nucleation, growth, coarsening, and agglomeration. The first method is widely applied in industries not only at the lab scale and it does not require complicated or expensive.

An analytic method typically starts with sample preparation and then continues to separation and detection. The selection of a sample preparation process is dependent on the following factors such as the analyte, analyte concentration level, sample matrix, instrumental measurement technique, and the required sample size. Atomic absorption, and inductively coupled plasma mass spectroscopy were used for determining the metals. Due to various mechanisms of extraction, co-precipitation methods may be able to overcome some limitations of the alternative way of extraction [91]. Co-precipitation is employed when direct precipitation is unable to separate the desired metallic species because of its low concentration in the sample solution. Co-precipitation may occur through metal adsorption on the precipitate surface or from metal adsorption into the precipitate structure.

Co-precipitation agents can be either organic or inorganic materials. The organic compounds that are typically chosen are those that can form neutral chelates with metallic species. Copper and Zinc are frequently used as the carrier element because of their low environmental impact.

Three main physical mechanisms contribute to the Co-precipitation process:

Surface adsorption

The surface charge on the precipitate can attract ions in a solution of the opposite charge.

Inclusion

The analyte may be incorporated non-isomorphically or isomorphically (mixed crystal) to replace an ion in the precipitate's crystal structure (solid solution)

Occlusion

Ions are physically enclosed in the forming precipitate before they can diffuse or be carried away.

The Co-precipitation method does not work well in cases where

i) the two reactants have different solubility in water
ii) the reactants do not precipitate at the same rate
iii) supersaturated solutions commonly occur [92].

While compared the co-precipitation method with other techniques it has very high supersaturation levels, low stability, solid phase formation, and chemical changes were observed during the aging of precipitation.

3.5. Characterization Studies

3.6. X-ray diffraction (XRD)

Max von Laue discovered in 1912 that crystalline materials react for X-ray wavelength as three-dimensional diffraction gratings similar to the spacing of the planes in a crystal lattice. X-ray diffraction is a frequently employed technique for investigating crystal structures and atomic intervals. Powdered XRD is the significant method to determine the crystal structure, lattice parameter, stress, and crystallite size of the nanoparticles. The typical photon energies of X-rays, which are electromagnetic radiation, range from 100 eV to 100 keV. Only X-rays with short wavelengths, from a few angstroms to 0.1 Å (1-120 keV), are used for diffraction applications.

3.6.1. Principle

The main principle is to fulfill the appropriate quality of experimental powder diffraction data is satisfying particle statistics. The XRD analysis is based on the diffraction phenomenon. The crystalline materials undergo a process of diffraction when the X-ray interacts with them. This occurs when the planes of the substance are separated by a distance of the same order of magnitude as the wavelength Cukα (1.5406 Å) radiation.

3.6.2. Working

When a monochromatic X-ray beam strikes a target material, the scattering of the X-rays from the target material's atoms is the primary reaction that takes place. The scattered X-rays are interfered with both constructively and destructively in crystalline materials with regular structures. This is called diffraction. The Bragg's law, $n\lambda = 2d\sin\theta$ where, n = 1, 2, 3, …. is the order of diffrection, λ is the wavelength of the radiation. Based on the 2Θ values, calculate the d-spacing for each diffraction peak. This method also calculates the typical distance between atomic layers or rows. The relation between the width of the X-ray diffraction line and crystallite size which is first derived by Debye - Scherrer in 1918 and the equation is known as the Scherrer equation.

$$D = \frac{k\lambda}{\beta \cos\theta}$$

where, D is the average crystallite size in nm

k = Scherrer's constant (0.9)

λ = wavelength of X-ray source

β = width at half maximum intensity

Θ = Bragg's angle

XRD determines the orientation of a single crystal or grain. It is useful to determine the crystal structure of an unknown material and quantify the dimensions, shapes, and internal stress of discrete crystalline areas [93].

3.6.3. X-Ray Diffraction Methods

(i) Laue's Photographic Method

Transmission Laue Method

The crystal is placed behind a film. It captures the beam that passes through the crystal and is recorded. The transmitted beam establishes the boundary of one side of the cone of Laue

reflections. The film always crosses the cone, and the spots caused by diffraction typically lie on an ellipse. The symmetry of a single crystal is determined using this method.

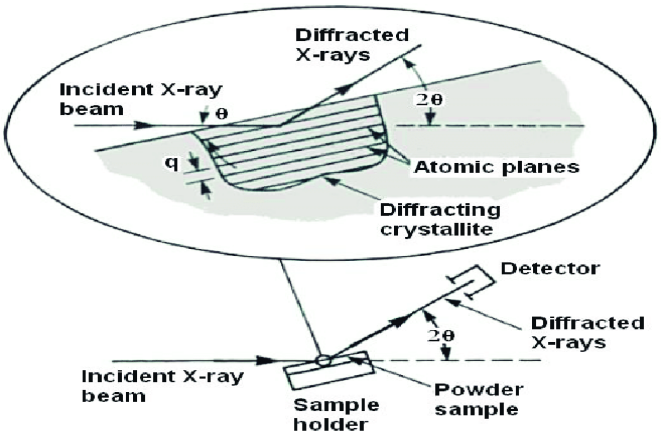

Fig. 3.5 Schematic diagram for X-ray powder diffraction (XRD)

Back Reflection Method

A film is positioned between the crystal and the X-ray source in the back reflection technique. The beams which are diffracted backward are recorded. The transmitted beam identifies the bottom of the cone of Laue reflections. The majority of the diffraction dots occupy a hyperbola while the film crosses the film. The back reflection method is the only method for the study of large and thick specimens.

(ii) Bragg's X-Ray spectrometer method

A single plane produces several diffraction lines. Diffraction patterns are determined by the sum of the diffraction lines. Also, the difference in distance between the planes can be derived from the pattern. The X-ray spectrum can be obtained by plotting a graph between the ionization current and the glancing angle. For various crystals, the ratios will differ. Experimentally observed ratios are compared with the calculated ratios the particular structure may be identified.

(iii) Rotating crystal method

Complete rotation method

In this method, each set of planes in a crystal diffracts four times during a single rotation. In the image's central focus, these beams are arranged in the rectangular pattern.

Oscillating method

An angle of 15° or 20° was the range of oscillation for the crystals. The crystal oscillates back and forth with the photographic plate. The spot's position on the plate indicates the crystal orientations at which it was produced.

(iv) Powder crystal method

The material under analysis is homogenized and finely powdered. The average bulk composition is then calculated. A gum piece is used to apply the fine powder on a hair that is suspended vertically in the axis of a cylindrical camera. When the monochromatic beam is allowed to pass many things could happen. There will be some particles in a fine powder that are not in the random orientation of small crystals. reflections are possible in different orders for each set. A different grain fraction will have a different collection of planes in the appropriate place for the reflections to appear.

3.6.4. Applications

i) XRD is a non-destructive method that helps to identify crystalline phases and orientation.
ii) It establishes structural characteristics, lattice parameters, strain, grain size, epitaxy, phase composition, optimal orientation (Laue), order-disorder transformation, and thermal expansion.
iii) It calculates the thickness of multilayers and thin films.

3.6.5. Limitation

i) Homogeneous and single-phase material is best for the identification of an unknown materials.
ii) The process requires tenths of a gram of material, which must be ground into a powder
iii) For mixed materials, the detection limit is ~2% of the sample
iv) Peak overlay may occur and worsens for high-angle "reflections".
v) For unit cell determinations, indexing of patterns for non-isometric crystal systems is complicated [94].

3.7. UV-vis Diffuse Reflectance Spectroscopy

UV-vis DRS is an effective method for analysing and characterizing the metal ion coordination. It is a non-destructive method that makes the interaction between light,

absorption, and scattering to create a unique reflectance spectrum that provides information about the structure and composition of the medium. Additionally, it provides information on the material's band gaps, particularly for semiconducting oxide.

3.7.1. Principle

When the ultraviolet radiation is absorbed, this results in the excitation of the electrons from the ground state towards a higher energy state there is the stimulation of an excited state by the molecule. By absorbing energy in the form of UV light, molecules with n-electrons can excite this electron to higher antibonding molecular orbitals. The direct and indirect band can be determined from the UV-Vis absorption or reflectance plot or Tauc plot by using the equation,

$$(\alpha.h\nu)^{n} = B\,(h\nu - E_g)$$

Where, α is the linear absorption coefficient, B is the proportionality constant, hν is the photon energy, E_g is the optical band gap and n is an index which the values 1/2 (direct), 3/2 (forbidden), 2 (indirect) depending on the nature of the electronic transition responsible for the reflection [95].

3.7.2. Working of UV-Vis spectrophotometer

The major components are:

1. Light source
2. Monochromator
3. Detector
4. Amplifier
5. Recorder

1. Light source

For visible light, a tungsten or halogen lamp is commonly used, whereas a deuterium lamp is generally used as the source of UV light. The instrument's light source must be changed during a measurement since UV and visible wavelengths require two separate light sources. The transition frequently takes place between 300 and 350 nm, where the light emission from both light sources is comparable and the transition may be achieved more easily.

2. Monochromator

It's generally composed of prism and slits. The rotating prism is used to emit the radiation that the primary source emits. The prism's rotation creates a series of wavelengths with increasing intensities to pass through the slits, selecting the various light source wavelengths that are separated by the prism for recording purposes. The monochromatic beam selected by the slit is further split into two beams with the help of another prism.

3. Detector

One of the photocells receives the beam from the sample cell and the second detector receives the beam from the reference. Compared to the sample cell beam, the reference cell radiation has a higher intensity. This leads to the photocells to generate pulsating or alternating currents.

4. Amplifier

The amplifier receives the alternating current produced by the photocells. A servo motor is connected to the amplifier. The current produced by photocells is typically of very low intensity, the amplifier's primary function is to amplify the signals many times so the signals are clear and accessible.

5. Recorder

A pen recorder that is connected to a computer is commonly paired with an amplifier. All the generated data is stored by the computer, which also produces the compound spectrum.

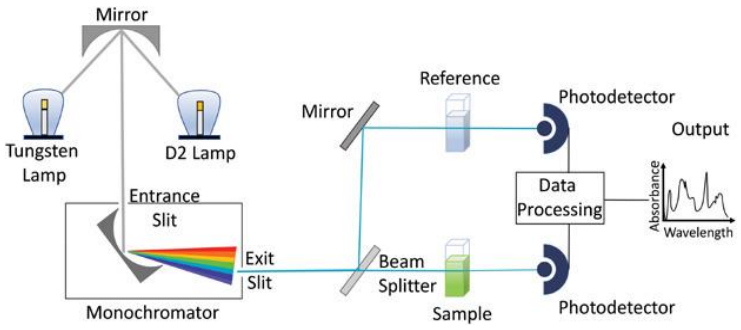

Fig. 3.6 Schematic representation of UV- vis spectrophotometer

3.7.3. Advantages

i) Versatility – A wide variety of samples including solids, liquids, and gases can be studied using UV-vis spectroscopy. Also, it can examine samples that are in different states, such as solutions, suspension, and emulsion.

ii) Low cost - The UV-Vis equipment is affordable, simple to use, and requires minimal maintenance

iii) High-resolution – Samples can be examined with great resolution using UV-Vis spectroscopy, allowing a through investigation of the sample.

iv) Wide range of applications – UV-Vis spectroscopy has numerous applications including analytical chemistry, biochemistry, material science, pharmaceuticals, food, water, and environmental analysis, etc., [96].

3.8. Fourier Transform Infrared Spectroscopy

FTIR stands for Fourier Transform Infra-Red. FTIR spectroscopy is the preferred method for the identification of chemical structures or functional groups in the materials. The frequency ranges are noted in the wavenumbers range of 4000 – 400 cm^{-1}. Some of the infrared radiation passes through the sample (transmitted) while some are absorbed by it which generates different vibration modes due to the excitation of molecules from a lower energy to the higher vibrational level energy. A molecular fingerprint of the material is produced by the resultant spectrum, which displays molecular absorption and transmission. Similar to a fingerprint, no two different chemical configurations emit the same infrared spectrum. This makes infrared spectroscopy useful for several kinds of analysis.

FTIR can provide the information,

- To identify unknown materials
- To determine the quality or consistency of a sample
- To determine the amount of components in a mixture

3.8.1. Working

A beam splitter separates an IR beam into two parts, with one reaching a fixed mirror and other and another mirror moving at a constant velocity. The two split beams are then reflected and recombined to create an interface pattern that reflects the constructive and destructive interface of the recombination. The sample is then sent to the interference pattern (also known as interferogram), and a detector is sent to the interferogram's transmitted portion. After comparing with a reference sample beam spectrum in the detector, a Fourier transform is acquired a complete spectrum as a function of wavenumber.

3.8.2. The Sample Analysis Process

1. The source

An illuminated black-body source emits infrared radiation. This bean travels via an aperture that regulates the energy delivered to the sample

2. The Interferometer

When the beam enters the interferometer where the “spectral encoding” occurs. The interferometer then releases the interferogram signal as a result.

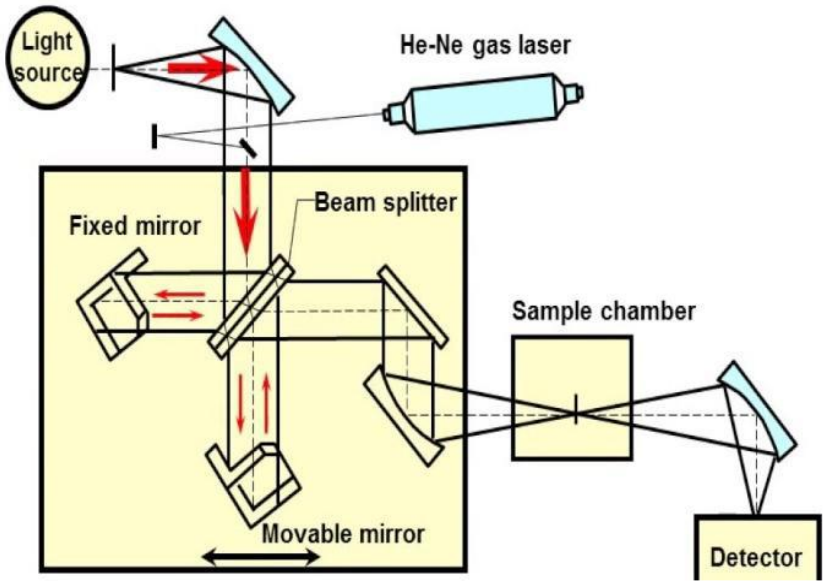

Fig. 3.7. Schematic diagram representation of FTIR

3. The sample

The beam enters the sample section where it is transmitted through or reflected off of the surface of the sample, depending on the type of analysis being achieved. The sample is specifically characterized by the absorption of particular frequencies of radiation in this range.

4. The Detector

Finally, the beam enters the detector for the final measurement. The detectors are particularly constructed to measure the distinctive interferogram signal.

5. The computer

The measured signals are converted to digital form and transferred to the computer, where it undergoes the Fourier transformation. The final infrared spectrum is then presented to the user for interpretation and any further manipulation.

3.8.3. Advantages

i) Speed: All the frequencies are recorded continuously, and a complete spectrum is measured in less than a second (felgett advantage)
ii) Sensitivity: In the interferometer, the radiation power transmitted onto the detector is very high which results in high sensitivity (Jacquinot advantage)
iii) Mechanical simplicity: The moving mirror in the interferometer is the only continuously moving part of the instrument. Thus, there is very little possibility of mechanical breakdown.
iv) FTIR collects all resolution elements with complete scans of the interferometer. Successful scans of the FTIR instrument are coded and averaged to enhance the signal to noise of the spectrum
v) Wavelength for the FTIR spectrum is very repeatable and reproducible and data can be compared to digital libraries for identification purposes [97].

3.9. Photoluminescence (PL) Spectroscopy

The photoluminescence works in a non-contact mode. It is a non-destructive technique for analysing the material's electronic structure. The radiation that an atom or molecule emits as a result of an electronic transition from a high energy level to a lower energy level is known as PL spectroscopy or emission spectroscopy.

3.9.1. Principle

When a material is stimulated, its electron occupies the allowable excited states. These excited electrons lose the excess energy by a radiative mechanism, which is known to produce light, or through a non-radiative process, which causes to revert to their equilibrium or ground state, which is stable. The emitted light energy is involved with the energy difference between two electronic states involved in the transition between the excited and equilibrium states. In comparison, the proportion of the radiative process determines the amount of light emitted.

3.9.2. Working

The electronic structure of the materials may be determined via PL spectroscopy. PL is a significant and contactless optical method employed to calculate purity and crystalline quality, and identify certain impurities in materials for energy devices. The Fig. 3.8 shows the schematic representation of the PL spectrometer setup. The setup consists of a PL spectrometer, an optical lens, a placeholder for the sample container, and a laser source.

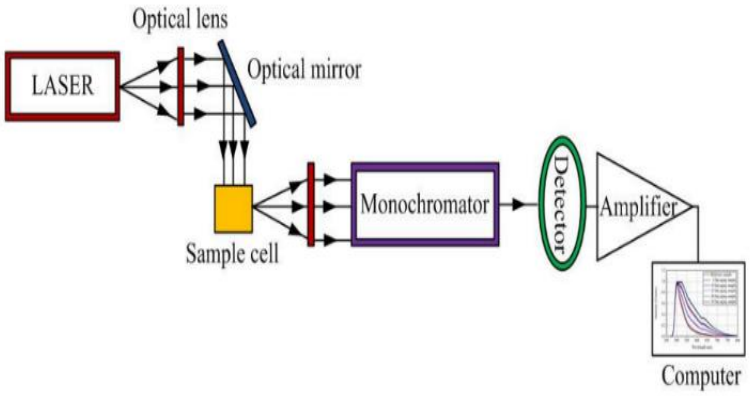

Fig. 3.8. Schematic diagram for the experimental setup of PL

The PL spectra were obtained as follows: the optical mirror, which focus the laser beam, launched by the laser source. Some electrons on the sample were excited to higher energy levels when the laser beam hit it. On their fall to their ground energy level, these electrons emitted radiation that was picked up by the PL spectrometer at particular wavelengths that represented the energy gradient between the two energy levels. The emission spectra intensity of the sample was then recorded as a function of wavelength using a PL spectrometer, which was used to separate the emitted light into its component wavelengths. [98, 99].

3.9.3. Advantages

i) high sensitivity
ii) good energy response
iii) reusability
iv) high resistance to high humidity and magnetic fields [100].

3.10. Scanning Electron Microscopy

The first commercial SEM was begun for bulk samples by Cambridge scientific instruments in 1965. Its resolution at that time was ~50 nm and now a day it is less than 1 nm. It was preliminary used to analyse the morphology of the samples, whereas now it is more of an analytical instrument. The important features of SEM include topography, morphology (shape and size of the particles), composition, and crystallographic information (how the atoms are arranged). With the help of a focussed electron beam, an SEM detects a rectangular area of the specimen to produce magnified images of it. This method is known as raster scanning. It is also known as a scanning electron microscope because the image is produced by moving a focused electron beam across the specimen's surface in a raster pattern.

3.10.1. Principle

The scanning electron microscope works on the principle of applying kinetic energy to produce signals on the interaction of the electrons. These electrons, which are used to examine crystallized elements and photons, are secondary electrons, backscattered electrons, and diffracted backscattered electrons. Secondary and backscattered electrons are used to produce an image. The secondary electrons emitted from the specimen play an important role in detecting the morphology and topography of the specimen while the backscattered electrons exhibit a contrast in the composition of the elements of the specimen.

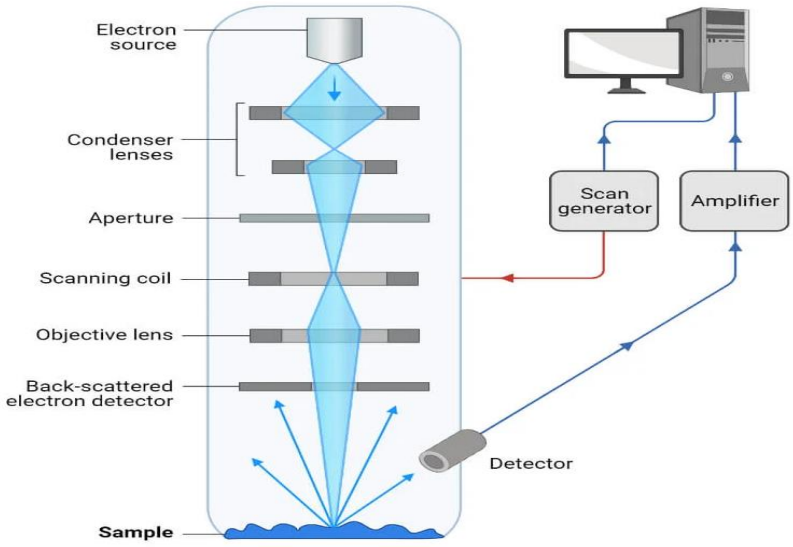

Fig. 3.9 Schematic ray diagram of SEM

3.10.2. Working

Tungsten filament lamps situated on the top of the column serve as the source of the electrons and the electromagnetic lenses, which are similar to those used in transmission electron microscopes. Thermal energy is provided to the electron source to cause the emission of electrons, which are then allowed to flow quickly to the anode, which is charged positively. The primary scattered (primary) electron emission at high energy levels and the secondary electron emission at low energy levels from the specimen surface are produced by the electron beam.

When the electron beam interacts with the specimen, it gives out signals that provide details about the specimen's surface topography and composition. Dried materials can be analysed directly, no special preparation is necessary for the specimen to be visible under the SEM. The structural characteristics of the cells must be maintained to avoid the cells from collapsing when exposed to the high vacuum of the microscope, hence microbial specimens must be fixed, dehydrated, and dried. The samples are mounted and coated with a thin layer of heavy metal elements to allow spatial scattering of electric charges on the surface of the specimen allowing better image production, with high clarity.

This microscope scans by tapering an electron beam back and forth over a narrow region of the microscope. When the electrons hit the specimen, the surface emits a small cluster of electrons, which are then recorded by a specialized detecting device. When the secondary electrons enter the detector, they hit a scintillator (a luminescence material that fluoresces when struck by a charged particle or high-energy photon). This provides rapid light flashes, which are converted into an electric current by a photomultiplier and transmitted as a signal to the cathode ray tube. This creates a viewable and photographable image that resembles a television image. The lifted surface receives high amounts of secondary electrons, which enter the detector, whereas depressed surfaces have fewer electrons reaching the surface, and as a result, fewer electrons enter the detector. The quantity of secondary electrons that enter the detector is greatly affected by the nature of the specimen. Therefore, the raised surface will show brighter and the depressed surface darker on the screen [101].

3.10.3. Applications

i) SEMs have numerous uses in a range of scientific and industrial fields.
ii) Scanning electron microscope can detect and analyse surface fractures, to provide information on microstructure, examine surface contaminations, display spatial variation in chemical compositions,
iii) SEM provides qualitative chemical analyses and identifies crystalline structures in addition to providing topographical, morphological, and compositional information.
iv) SEMs can be an essential research tool in fields such as life science, biology, gemology, medical and forensic science, and metallurgy.
v) SEMs can also be used for industrial and technological activities like semiconductor inspection, manufacturing miniscule products on a production path, and assembling computer clips

3.10.4. Advantages

i) SEMs are easy to operate with the proper training and advances in computer technology and associated software make operation user-friendly.
ii) The instrument works faster, often completing SEI, BSE, and EDS analyses in less than five minutes.
iii) Modern SEMs allow for the generation of data in digital form. Although all prepared samples are placed in the vacuum chamber, most SEM samples require minimal preparation actions [102].

CHAPTER IV

RESULTS AND DISCUSSION

4.1. Introduction

ZnO is a promising material with a wide range of applications in photonics, optoelectronics, gas sensing, field emission, piezoelectricity etc., ZnO is a semiconductor with a large bandgap (3.37eV) and high exciton binding energy (60 MeV). Due to its unique features such as wide and direct band gap near the UV region, strong oxidation capacity, excellent photocatalytic behavior and a major free-exciton binding energy that results in an excitonic emission can endure at room temperature or above room temperature. ZnO is also a chemically stable and environmentally friendly material and without modification it is used in biomedical applications. This chapter describes the study of pure and doped ZnO particles synthesized by the co-precipitation method and discussion on the as-synthesized samples on different techniques viz. X-ray diffraction (XRD), UV-Visible spectroscopy (UV-Vis), Fourier transformation infrared spectroscopy (FTIR).

4.2. Synthesis of pure and Cobalt doped ZnO nanoparticles

4.2.1. ZnO synthesis

Synthesis of pure ZnO particles by a co-precipitation method using an aqueous solution of zinc acetate dihydrate [$Zn(CH_3COO)_2.2H_2O$] and sodium hydroxide [NaOH]. In the synthesis process, the required amount of zinc acetate dihydrare is fully dissolved in deionized water, and a determined quality of aqueous NaOH solution was added into the mixture in drops to maintain the pH~10. Later, the solution containing the white precipitate is stirred at room temperature for 3 hrs and the resulting substance is aged for 24h and centrifuged the solution at 2000 rpm. A white precipitate is obtained and it is washed several times with distilled water and finally, the precipitate is dried at 500°C for 2 h.

4.2.2. Co-doped ZnO synthesis

To synthesize Co-doped ZnO particles, the required amount of cobalt acetate (2.5 %) in water was mixed with a zinc acetate solution. The solution was stirred continuously for 1h and the calculated amount of aqueous NaOH solution was added drop by drop to the homogeneous mixture until the pH value of the solution reaches ~10 and the obtained pale blue

precipitate was stirred for 3h. The precipitate was aged for 24h at ambient temperature, followed by centrifuging (2000 rpm), filtering and washing several times with deionized water. The synthesized samples are dried at 400°C, 500°C, 600°C for 2hrs.

4.3. Structural studies (XRD)

X-ray diffraction (XRD) measurements are employed to investigate the crystal structure and average size of ZnO samples and evaluate the phase purity. XRD characteristics pattern of ZnO and 2.5% Co doped ZnO particles obtained at different annealed temperatures by the co-precipitation method are shown in Fig. 4.1. The crystallite size of undoped ZnO and Co doped ZnO particles are estimated by applying the Scherrer equation. The half intensity width of the planes (100), (002) and (101) are taken to calculate the crystallite size using Scherrer equation, is given in chapter 3.

The average crystallite size is found to be 23 nm for pure ZnO and 27 nm, 30 nm, 30.8 nm for 2.5% cobalt doped ZnO annealed at 400°C, 500°C, 600°C respectively. It is seen that, when compared with undoped ZnO, cobalt doped ZnO samples have an increase in crystalline size. By increasing the temperature, values of lattice parameter a, c decreases compared to ZnO particles. XRD patterns of all samples exhibit sharp and intense peak indicates that the samples are highly crystalline. The XRD peaks for (100), (002), (101), (012), (110), (111), (013), (200), (112), (201), (004) and (202) planes indicate the formation of pure wurtzite phase of ZnO. particularly the fast anisotropic growth along (101) direction confirm the formation of hexagonal wurtzite structure (JCPDS file number: 800075). No impurities are detected, which shows formation of high purity ZnO particles. The sharp diffraction peaks clearly resemble good crystalline nature of the particles. As the annealing temperature increases, Co-doped ZnO particles become more crystalline when compared to ZnO particles These results indicate that Co ions have successfully occupied the lattice site of ZnO rather than the interstitial ones.

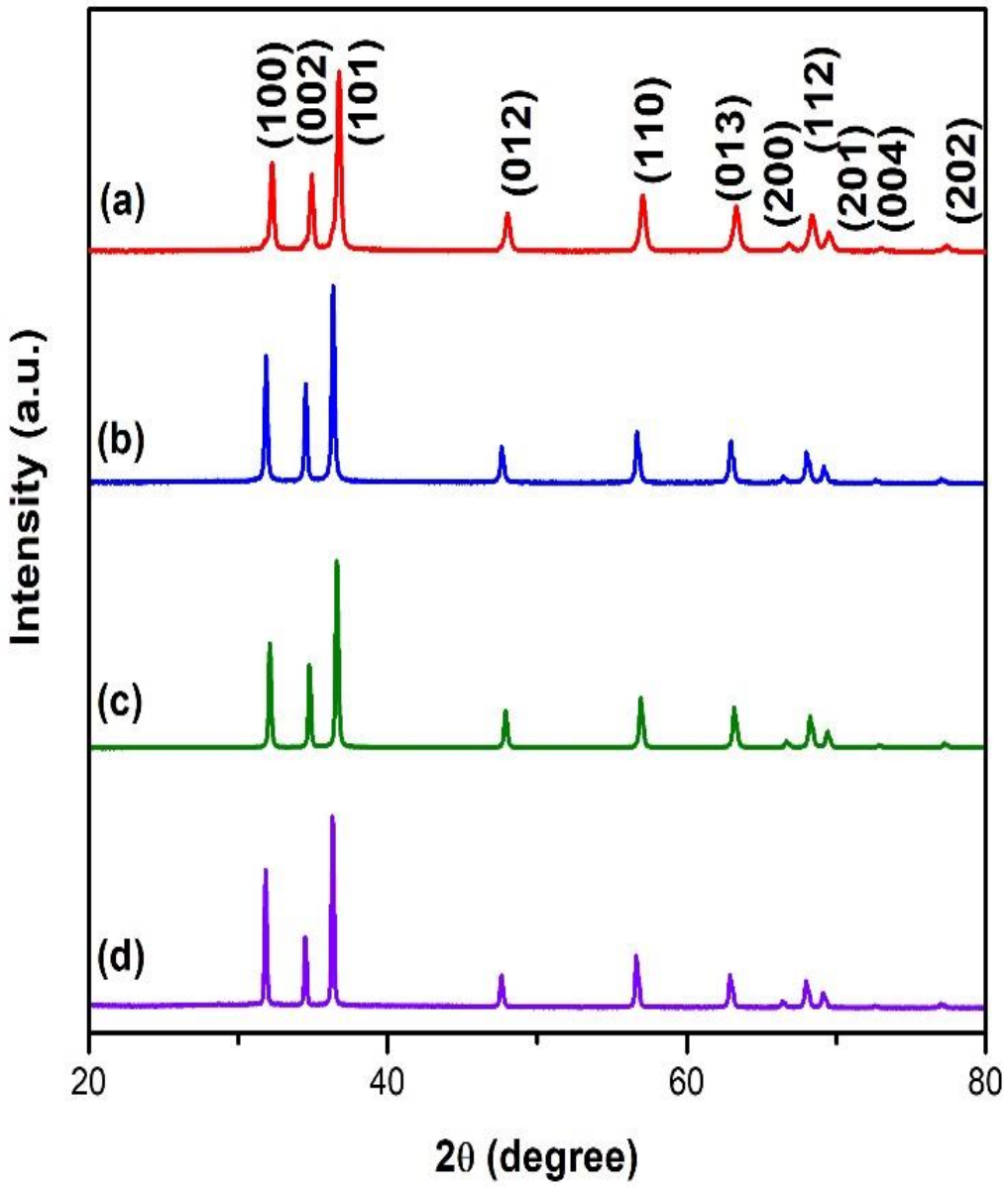

Fig. 4.1 Powder X-ray diffraction patterns of (a) ZnO, (b) Co-doped ZnO at 400°C (c) 500°C (d) 600°C annealing temperatures

4.4. UV–Vis Transmission Spectra analysis

Fig. 4.2 shows the UV-vis DRS of ZnO and Co- doped ZnO. The absorption edge of ZnO, 2.5% of Co-ZnO at different annealing temperatures 400°C, 500°C, 600°C are observed at 451 nm, 453 nm, 459 nm, 467 nm respectively. The Tauc method is based on the assumption that the energy-dependent absorption coefficient α which is given in chapter 3.

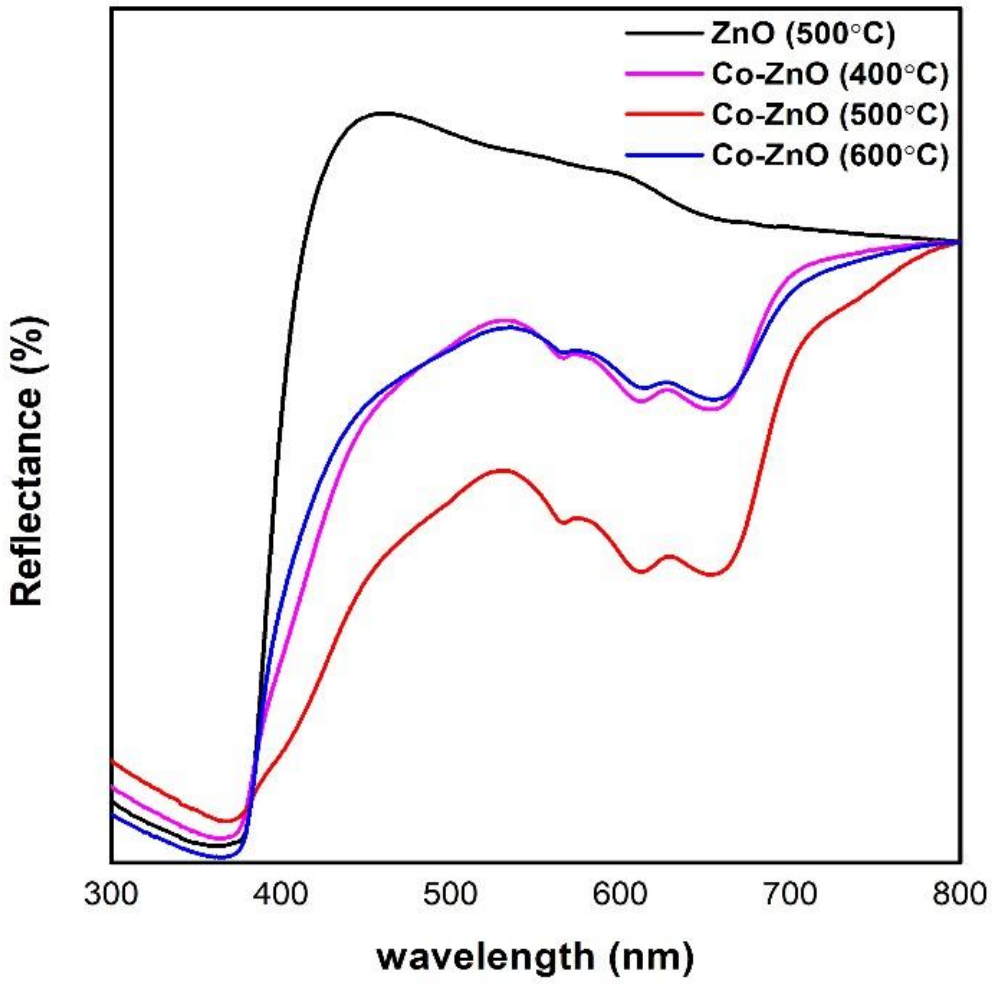

Fig. 4.2 Diffuse Reflectance Spectra (DRS) of ZnO and Co doped ZnO at annealed temperatures of 400°C, 500°C, 600°C

The energy of band gap (E_g) is the sample can be estimated from a plot $(\alpha h\nu)^{1/2}$ versus energy ($h\nu$) [103]. The optical E_g values is found to gradually decreases from 3.15 eV for ZnO to 3.06 eV for Co-ZnO at 400°C, 2.96 eV for 500°C, 2.73 eV for 600°C respectively [36] which is shown in Fig. 4.3

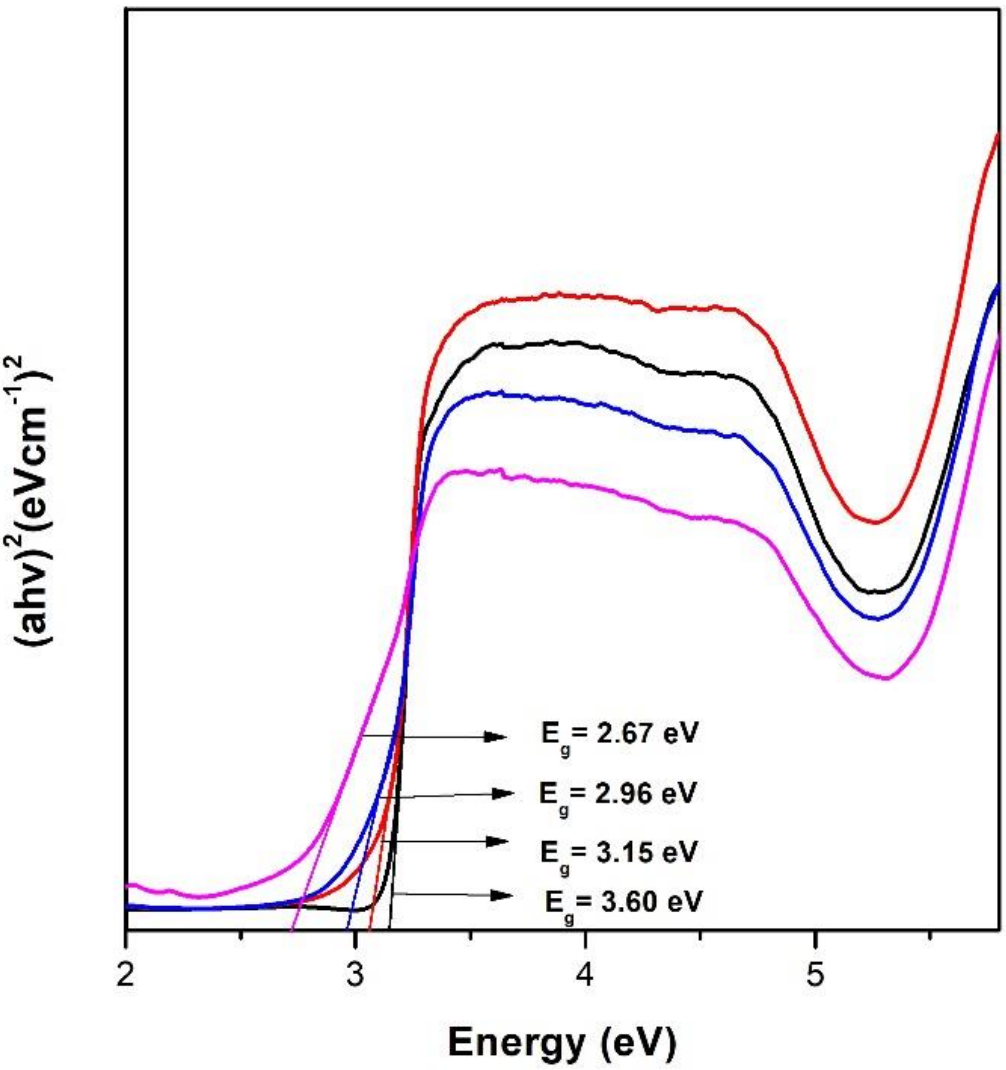

Fig. 4.3 $(\alpha h\nu)^2$ versus hν plot for ZnO and Co doped ZnO showing the optical band gap

4.5. Fourier transformation infrared spectroscopy (FTIR)

FTIR is a useful technique to determine the information about chemical bonding, vibration position, chemical composition and mismatching of the samples. The FTIR spectra of pure and Co - doped ZnO particles at various annealing temperatures are shown in Fig. 4.4. The spectra shows the Zn-O bond appear at around 450–490 cm^{-1}. The band at around 490 cm^{-1} may be related with oxygen vacancy or oxygen deficiency in ZnO. The absorption peak at 554 cm^{-1} corresponds to the stretching vibration of Zn–O bond.

The vibration around 613–668 cm^{-1} corresponds to the C–C group. The peaks from 700 to 900cm−1 are attributed to the bond between cobalt and oxygen (Co-O). The weak band around 870 cm-1 is attributed to the metal– oxygen vibration frequency due to the changes in the nanostructural features by the doping of Co into the Zn–O lattice. The peaks observed in the range of 3350–3750 cm^{-1} corresponds to the O–H stretching vibration of water molecule indicates adsorption of moisture contents on the surface of the sample [21, 36, 77].

Vibrational frequencies (cm^{-1})	**Spectral assignment**
450 - 490	Zn-O
490	O vacancies/ oxygen deficiency in ZnO
554	Stretching vibration of Zn-O bond
613 - 668	C-C group
700 - 900	Co-O
870	Metal-oxygen vibration frequency
3350 - 3750	O-H stretching vibration

Table 4.1 Fourier Transform Infrared Spectroscopy spectral assignment for prepared samples of ZnO and Co-ZnO.

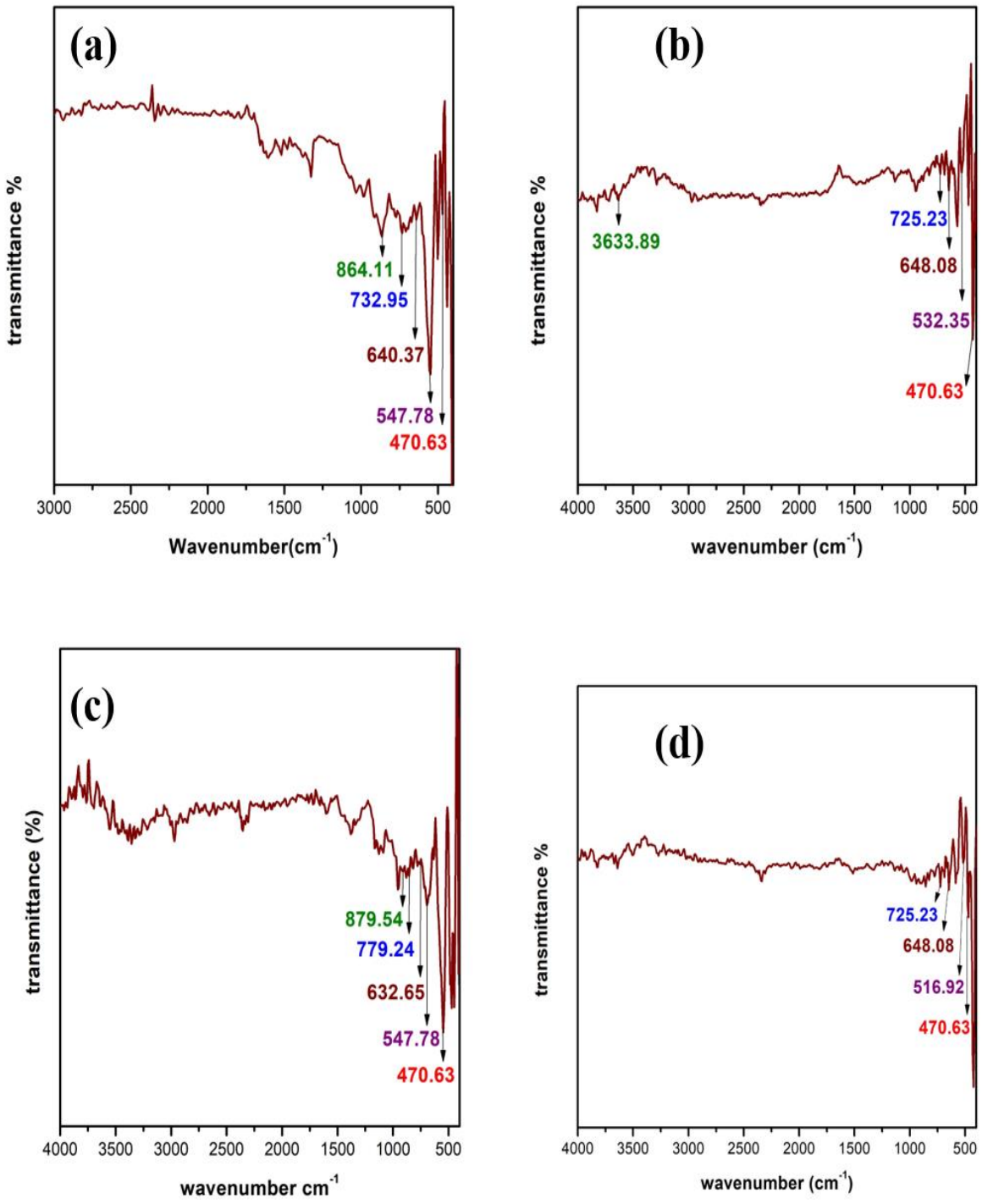

Fig. 4.4 FTIR spectra of (a) ZnO at 500°C and Co-doped ZnO at various annealed temperatures of (b) 400°C (c) 500°C (d) 600°C

CHAPTER V

SUMMARY AND CONCLUSION

In this present study, ZnO and Co-doped ZnO is synthesized using co-precipitation method. XRD spectra clearly confirm the incorporation of Co^{2+} ions into the lattice site of Zn^{2+} ions in the host ZnO matrix and confirms the wurtzite structure. FTIR spectra show the occurrence of some functional groups that merely comes from reagent used during the synthesis process. UV-absorption spectrum showed blue shift in wavelength for Cobalt doped sample as compared with pure ZnO nanoparticles sample. Decrease in band gap proved the successful incorporation of Co^{2+} ions in ZnO matrix. Due to soft magnetization offered by Co doped ZnO samples, as potential candidate for spintronics applications. The prepared samples are to be further studied for photoluminescence study and morphological analysis in order to confirm the oxygen vacancies and microstructure respectively. Further photocatalytic activity of the prepared ZnO and Co-doped ZnO to be studied.

REFERENCES

[1] Britannica, T. (2022). semiconductors. *Argon. Encyclopedia Britannica*.

[2] https://www.geeksforgeeks.org/definition-and-classification-of-energy-bands/

[3] Linsebigler, A. L., Lu, G., & Yates Jr, J. T. (1995). Photocatalysis on TiO2 surfaces: principles, mechanisms, and selected results. *Chemical reviews*, *95*(3), 735-758.

[4] S.L.Gupta,V.Kumar, (2007). Solid State Physics, NeerajGupta, K.Nath&Co.

[5] S.O.Pillai, (2015). Solid State Physics, New age international (P) Ltd.

[6] Kumar, A., Richhariya, G., & Sharma, A. (2015). Solar photovoltaic technology and its sustainability. *Energy sustainability through green energy*, 3-25.

[7] Siddiqi, G., Pan, Z., & Hu, S. (2017). III–V semiconductor photoelectrodes. In *Semiconductors and Semimetals* (Vol. 97, pp. 81-138). Elsevier.

[8] Makuła, P., Pacia, M., & Macyk, W. (2018). How to correctly determine the band gap energy of modified semiconductor photocatalysts based on UV–Vis spectra. *The journal of physical chemistry letters*, *9*(23), 6814-6817.

[9] Gupta, V. K., Ali, I., Saleh, T. A., Nayak, A., & Agarwal, S. (2012). Chemical treatment technologies for waste-water recycling—an overview. *Rsc Advances*, *2*(16), 6380-6388.

[10] Jo, W. K., & Tayade, R. J. (2014). Recent developments in photocatalytic dye degradation upon irradiation with energy-efficient light emitting diodes. *Chinese Journal of Catalysis*, *35*(11), 1781-1792.

[11] Santhosh, C., Malathi, A., Daneshvar, E., Kollu, P., & Bhatnagar, A. (2018). Photocatalytic degradation of toxic aquatic pollutants by novel magnetic 3D-TiO2@ HPGA nanocomposite. *Scientific reports*, *8*(1), 1-15.

[12] Baruah, A., Chaudhary, V., Malik, R., & Tomer, V. K. (2019). Nanotechnology based solutions for wastewater treatment. In *Nanotechnology in Water and wastewater treatment* (pp. 337-368). Elsevier.

[13] Ajmal, A., Majeed, I., Malik, R. N., Idriss, H., & Nadeem, M. A. (2014). Principles and mechanisms of photocatalytic dye degradation on TiO2 based photocatalysts: a comparative overview. RSC Adv 4: 37003–37026.

[14] Saravanan, A., Kumar, P. S., Jeevanantham, S., Karishma, S., Tajsabreen, B., Yaashikaa, P. R., & Reshma, B. (2021). Effective water/wastewater treatment methodologies for toxic pollutants removal: Processes and applications towards sustainable development. *Chemosphere*, *280*, 130595.

[15] Tatarchuk, T., Peter, A., Al-Najar, B., Vijaya, J., & Bououdina, M. (2018). Photocatalysis: activity of nanomaterials. *Nanotechnology in environmental science*, 209-292.

[16] Ren, G., Han, H., Wang, Y., Liu, S., Zhao, J., Meng, X., & Li, Z. (2021). Recent advances of photocatalytic application in water treatment: A review. *Nanomaterials*, *11*(7), 1804.

[17] Nakata K, Fujishima A, J Photochem Photobiol C., 13 (2012) 169–189.

[18] Ivanova, T., Harizanova, A., Koutzarova, T., Vertruyen, B., and Closset, R. (2020). Structural and optical characterization of nitrogen and gallium co-doped ZnO thin films, deposited by sol-gel method. *Journal of Molecular Structure*, 1206, 127773.

[19] Weldegebrieal, G. K. (2020). Synthesis method, antibacterial and photocatalytic activity of ZnO nanoparticles for azo dyes in wastewater treatment: A review. *Inorganic Chemistry Communications*, 120, 108140.

[20] Singh, K., Kaur, H., Sharma, P. K., Singh, G., and Singh, J. (2023). ZnO and cobalt decorated ZnO NPs: Synthesis, photocatalysis and antimicrobial applications. *Chemosphere*, 313, 137322.

[21] Rajwali Khan, Ihab Shigidi, Sattam Al Otaibi, Khaled Althubeiti, Sherzod Shukhratovich Abdullaev, Nasir Rahman, Mohammad sohail, Alamzeb Khan, Shahid Iqbal,Tommaso Del Rosso,Quaid Zaman and Aurangzeb Khan, "Room temperature dilute magnetic semiconductor response in (Gd, Co) co-doped ZnO for efficient spintronics applications", *RSC Adv*, **12**, 36126 (2022).

[22] Huong, P. T. L., Van Quang, N., Tran, M. T., Trung, D. Q., Hop, D. T. B., Tam, T. T. H., ... and Dao, V. D. (2022). Excellent visible light photocatalytic degradation and mechanism insight of Co2+-doped ZnO nanoparticles. *Applied Physics A*, 128(1), 24.

[23] Adeel, M., Saeed, M., Khan, I., Muneer, M., and Akram, N. (2021). Synthesis and characterization of Co–ZnO and evaluation of its photocatalytic activity for photodegradation of methyl orange. *ACS omega*, 6(2), 1426-1435.

[24] Alanazi, H. S., Ahmad, N., and Alharthi, F. A. (2021). Synthesis of Gd/N co-doped ZnO for enhanced UV-vis and direct solar-light-driven photocatalytic degradation. *RSC advances*, 11(17), 10194-10202.

[25] Wahba, M. A., Yakout, S. M., and Khaled, R. (2021). Interface engineered efficient visible light photocatalytic activity of MWCNTs/Co doped ZnO nanocomposites: Morphological, optical, electrical and magnetic properties. *Optical Materials*, 115, 111039.

[26] Chai, C., Liu, H., and Yu, W. (2021). The electronic and optical properties of the Fe, Co, Ni and Cu doped ZnO monolayer photocatalyst. Chemical Physics Letters, 778, 138765.

[27] S. Vinoth, A. M. S. Arulanantham, S. Saravanakumar, R. S. Rimal Isaac, N. Soundaram, N. Chidhambaram, Devarajan Alagarasan, S. Varadharajaperumal, Mohd. Shkir and S. Al Faify, "Enriched optoelectronic properties of cobalt-doped ZnO thin films for photodetector applications", *J Mater Sci: Mater Electron*, **32**, 27060–27072 (2021).

[28] Aswathi K. Sivan, Alejandro Gal´an-Gonz´alez, Lorenzo Di Mario, Nicolas Tappy, Javier Hern´andez-Ferrer, Daniele Catone, Stefano Turchini, Ana M. Benito, Wolfgang K. Maser, Simon Escobar Steinvall, Anna Fontcuberta i Morral, Andrew Gallant, Dagou A. Zeze, Del Atkinson and Faustino Martelli, "Optical properties and carrier dynamics in Codoped ZnO nanorods", *Nanoscale Adv*, 3, 214 (2021).

[29] Tanji, K., Zouheir, M., Hachhach, M., Ahmoum, H., Jellal, I., Masaoudi, H. E., ... and Kherbeche, A. (2021). Design and simulation of a photocatalysis reactor for rhodamine B degradation using cobalt-doped ZnO film. *Reaction Kinetics, Mechanisms and Catalysis*, 134, 1017-1038.

[30] Habanjar, K., Almoussawi, M., Abdallah, A. M., and Awad, R. (2020). Magneto-optical effect of (Sm, Co) co-doping in ZnO semiconductor. *Physica B: Condensed Matter*, 598, 412444.

[31] Wang, Y., Ge, S., Cheng, W., Hu, Z., Shao, Q., Wang, X., ... and Guo, Z. (2020). Microwave hydrothermally synthesized metal–organic framework-5 derived C-doped ZnO with enhanced photocatalytic degradation of rhodamine B. *Langmuir*, 36(33), 9658-9667.

[32] Akhtar, J., Tahir, M. B., Sagir, M., and Bamufleh, H. S. (2020). Improved photocatalytic performance of Gd and Nd co-doped ZnO nanorods for the degradation of methylene blue. *Ceramics International*, 46(8), 11955-11961.

[33] Jyothi, N. S., and Ravichandran, K. (2020). Optimum pH for effective dye degradation: Mo, Mn, Co and Cu doped ZnO photocatalysts in thin film form. *Ceramics International*, 46(14), 23289- 23292.

[34] Ahmad, I., Akhtar, M. S., Ahmed, E., Ahmad, M., Keller, V., Khan, W. Q., and Khalid, N. R. (2020). Rare earth co-doped ZnO photocatalysts: Solution combustion synthesis and environmental applications. *Separation and Purification Technology*, 237, 116328.

[35] Satdeve, N. S., Ugwekar, R. P., and Bhanvase, B. A. (2019). Ultrasound assisted preparation and characterization of Ag supported on ZnO nanoparticles for visible light degradation of methylene blue dye. *Journal of Molecular Liquids*, 291, 111313.

[36] Chauhan, N., Singh, V., Kumar, S., Sirohi, K., and Siwatch, S. (2019). Synthesis of nitrogen-and cobalt-doped rod-like mesoporous ZnO nanostructures to study their photocatalytic activity. *Journal of Sol-Gel Science and Technology*, 91, 567-577.

[37] Liu, H., Zhong, L., Govindaraju, S., and Yun, K. (2019). ZnO rod decorated with Ag nanoparticles for enhanced photocatalytic degradation of methylene blue. *Journal of Physics and Chemistry of Solids*, 129, 46-53.

[38] Zhang, L., Zhu, X., Wang, Z., Yun, S., Guo, T., Zhang, J., ... and Chen, J. (2019). Synthesis of ZnO doped high valence S element and study of photogenerated charges properties. *RSC advances*, 9(8), 4422-4427.

[39] Farhadian, N., Akbarzadeh, R., Pirsaheb, M., Jen, T. C., Fakhri, Y., and Asadi, A. (2019). Chitosan modified N, S-doped TiO2 and N, S-doped ZnO for visible light photocatalytic degradation of tetracycline. *International journal of biological macromolecules*, 132, 360-373.

[40] Prabakaran, E., and Pillay, K. (2019). Synthesis of N-doped ZnO nanoparticles with cabbage morphology as a catalyst for the efficient photocatalytic degradation of methylene blue under UV and visible light. *RSC advances*, 9(13), 7509-7535.

[41] Faraz, M., Naqvi, F. K., Shakir, M., and Khare, N. (2018). Synthesis of samarium-doped zinc oxide nanoparticles with improved photocatalytic performance and recyclability under visible light irradiation. *New Journal of Chemistry*, 42(3), 2295-2305.

[42] Liu, L., Liu, Z., Yang, Y., Geng, M., Zou, Y., Shahzad, M. B., ... and Qi, Y. (2018). Photocatalytic properties of Fe-doped ZnO electrospun nanofibers. *Ceramics International*, 44(16), 19998- 20005.

[43] Arshad, M., Qayyum, A., Abbas, G., Haider, R., Iqbal, M., and Nazir, A. (2018). Influence of different solvents on portrayal and photocatalytic activity of tin-doped zinc oxide nanoparticles. *Journal of Molecular Liquids*, 260, 272-278.

[44] Pascariu, P., Tudose, I. V., Suchea, M., Koudoumas, E., Fifere, N., and Airinei, A. (2018). Preparation and characterization of Ni, Co doped ZnO nanoparticles for photocatalytic applications. *Applied surface science*, 448, 481-488.

[45] Vaiano, V., Matarangolo, M., Murcia, J. J., Rojas, H., Navío, J. A., and Hidalgo, M. C. (2018). Enhanced photocatalytic removal of phenol from aqueous solutions using ZnO modified with Ag. *Applied Catalysis B: Environmental*, 225, 197-206.

[46] Pessoni, H. V., Banerjee, P., and Franco, A. (2018). Colossal dielectric permittivity in Co-doped ZnO ceramics prepared by a pressure-less sintering method. *Physical Chemistry Chemical Physics*, 20(45), 28712-28719.

[47] Potter, D. B., Powell, M. J., Parkin, I. P., and Carmalt, C. J. (2018). Aluminium/gallium, indium/gallium, and aluminium/indium co-doped ZnO thin films deposited via aerosol assisted CVD. *Journal of Materials Chemistry C*, 6(3), 588-597.

[48] Narasimman, S., Balakrishnan, L., and Alex, Z. C. (2018). Fiber optic magnetic field sensor using Co doped ZnO nanorods as cladding. *RSC advances*, 8(33), 18243-18251.

[49] Mimouni, R., Souissi, A., Madouri, A., Boubaker, K., and Amlouk, M. (2017). High photocatalytic efficiency and stability of chromium-indium codoped ZnO thin films under sunlight irradiation for water purification development purposes. *Current Applied Physics*, 17(8), 1058-1065.

[50] Sutanto, H., Wibowo, S., Arifin, M., and Hidayanto, E. (2017). Photocatalytic activity of cobalt- doped zinc oxide thin film prepared using the spray coating technique. *Materials Research Express*, 4(7), 076409.

[51] Dai, G., Qin, H., Zhou, H., Wang, W., and Luo, T. (2018). Template-free fabrication of hierarchical macro/mesoporpous SnS2/TiO2 composite with enhanced photocatalytic degradation of Methyl Orange (MO). *Applied Surface Science*, 430, 488-495.

[52] SivaKarthik, P., Thangaraj, V., Kumaresan, S., and Vallalperuman, K. (2017). Comparative study of Co and Ni substituted ZnO nanoparticles: synthesis, structural, optical and photocatalytic activity. *Journal of Materials Science: Materials in Electronics*, 28, 10582-10588.

[53] Rana, S. B., Singh, R. P. P., and Arya, S. (2017). Structural, optical, magnetic and antibacterial study of pure and cobalt doped ZnO nanoparticles. *Journal of Materials Science: Materials in Electronics*, 28, 2660-2672.

[54] Dhatshanamurthi, P., and Shanthi, M. (2016). Li and Ag Co-Doped ZnO Photocatalyst for Degradation of RO 4 Dye Under Solar Light Irradiation. *Journal of Nanoscience and Nanotechnology*, 16(6), 5913-5922.

[55] Zhou, Y., Chen, G., Yu, Y., Zhao, L., Yu, Q., and He, Q. (2016). Effects of La-doping on charge separation behavior of ZnO: GaN for its enhanced photocatalytic performance. *Catalysis Science and* Technology, 6(4), 1033-1041.

[56] Prabhakar Vattikuti, S. V., Byon, C., and Reddy, C. V. (2016). ZrO 2/MoS 2 heterojunction photocatalysts for efficient photocatalytic degradation of methyl orange. *Electronic Materials Letters*, 12, 812-823.

[57] Chunxiao Lu, Yang Chen, Hongbo Zhang, Liang Tang, Shengnan Wei, Yahui Song & Jun Wang , "Preparation of Er^{3+}:$YAlO_3$/Fe- and Co-doped TiO_2–ZnO coated composites and their visible-light photocatalytic activity in degradation of some organic dyes" *Res. Chem. Intermed*., 42, 4651-4668 (2016).

[58] Manikandan, A. S., Renukadevi, K. B., Ravichandran, K., Rajkumar, P. V., and Boubaker, K. (2016). Enhanced photocatalytic, antibacterial and magnetic properties of ZnO nanopowders through lattice compatible cobalt doping. *Journal of Materials Science: Materials in Electronics*, 27, 11890-11901.

[59] Gupta, R., Eswar, N. K., Modak, J. M., and Madras, G. (2016). Visible light driven efficient N and Cu co-doped ZnO for photoinactivation of Escherichia coli. *RSC advances*, 6(89), 85675-85687.

[60] Alshammari, A. S., Chi, L., Chen, X., Bagabas, A., Kramer, D., Alromaeh, A., and Jiang, Z. (2015). Visible-light photocatalysis on C-doped ZnO derived from polymer-assisted pyrolysis. *RSC advances*, 5(35), 27690-27698.

[61] El Ghoul, J., Kraini, M., Lemine, O. M., and El Mir, L. (2015). Sol–gel synthesis, structural, optical and magnetic properties of Co-doped ZnO nanoparticles. *Journal of Materials Science: Materials in Electronics*, 26, 2614-2621.

[62] Fettkenhauer, C., Wang, X., Kailasam, K., Antonietti, M., and Dontsova, D. (2015). Synthesis of efficient photocatalysts for water oxidation and dye degradation reactions using CoCl 2 eutectics. *Journal of Materials Chemistry A*, 3(42), 21227-21232.

[63] J. J Macías*i*-Sánchez, L. Hinojosa-Reyes, A. Caballero-Quintero, W. de la Cruz, E. Ruiz-Ruiz, A. Hernández-Ramírez , and J. L. Guzmán-Mar , "Synthesis of nitrogen-dopsol–gel by sol–gel method: characterization and its application on visible photocatalytic degradation of 2,4-D and picloram herbicides", *Photochem. Photobiol. Sci***,** 14, 536-542 (2015).

[64] Agorku, E. S., Mamo, M. A., Mamba, B. B., Pandey, A. C., and Mishra, A. K. (2015). Cobalt-doped ZnS-reduced graphene oxide nanocomposite as an advanced photocatalytic material. *Journal of Porous Materials*, 22, 47-56.

[65] Gandhi, V., Ganesan, R., Abdulrahman Syedahamed, H. H., and Thaiyan, M. (2014). Effect of cobalt doping on structural, optical, and magnetic properties of ZnO

nanoparticles synthesized by coprecipitation method. *The Journal of Physical Chemistry C*, 118(18), 9715-9725.

[66] Wang, C. Y., Ma, S. Y., Li, F. M., Chen, Y., Xu, X. L., Wang, T., ... and Zhu, J. (2014). The effect of Mg and Al co-doping on the structural and photoelectric properties of ZnO thin film. *Materials science in semiconductor processing*, 17, 27-32.

[67] Nam, G., Yoon, H., Kim, B., Lee, D. Y., Kim, J. S., and Leem, J. Y. (2014). Effect of Co doping concentration on structural properties and optical parameters of Co-doped ZnO thin films by sol–gel dip-coating method. *Journal of Nanoscience and Nanotechnology*, 14(11), 8544-8548.

[68] Mesaros, A., Ghitulica, C. D., Popa, M., Mereu, R., Popa, A., Petrisor Jr, T., ... and Vasile, B. S. (2014). Synthesis, structural and morphological characteristics, magnetic and optical properties of Co doped ZnO nanoparticles. *Ceramics International*, 40(2), 2835-2846.

[69] Michele Karoline Lima, Daniela Martins Fernandes, Marcela Fernandes Silva, Mauro Luciano Baesso, Antonio Medina Neto, Gutierrez Rodrigueˆs de Morais, Celso Vataru Nakamura, Angelo de Oliveira Caleare, Ana Adelina Winkler Hechenleitner, Edgardo Alfonso Go´mez Pineda, "Co-doped ZnO nanoparticles synthesized by an adapted sol–gel method: effects on the structural, optical, photocatalytic and antibacterial properties", *J Sol-Gel Sci Technol*, **72**, 301–309, (2014).

[70] Poongodi, G., Kumar, R. M., andJayavel, R. (2014). Influence of S doping on structural, optical and visible light photocatalytic activity of ZnO thin films. *Ceramics International*, 40(9), 14733-14740.

[71] Kuriakose, S., Satpati, B., andMohapatra, S. (2014). Enhanced photocatalytic activity of Co doped ZnO nanodisks and nanorods prepared by a facile wet chemical method. *Physical Chemistry Chemical Physics*, 16(25), 12741-12749.

[72] Sun, S., Chang, X., Li, X., and Li, Z. (2013). Synthesis of N-doped ZnO nanoparticles with improved photocatalytical activity. *Ceramics International*, 39(5), 5197-5203.

[73] Li, X., Li, J. H., Li, S. J., Fang, X., Fang, F., Chu, X. Y., ...and Hu, J. X. (2013). Fabrication and visible light photocatalytic activity of Co-doped ZnO nanorods. *Chemical Research in Chinese Universities*, 29(6), 1032-1035.

[74] 57.Siddheswaran, R., Mangalaraja, R. V., Gómez, M. E., Avila, R. E., andJeyanthi, C. E. (2013). Room temperature ferromagnetism in combustion synthesized nanocrystalline Co, Al co-doped ZnO. Journal of alloys and compounds, 581, 146-149.

[75] Lin, Y. G., Hsu, Y. K., Chen, Y. C., Chen, L. C., Chen, S. Y., and Chen, K. H. (2012). Visible- light-driven photocatalytic carbon-doped porous ZnO nanoarchitectures for solar water- splitting. *Nanoscale*, 4(20), 6515-6519.

[76] Ma, H., Yue, L., Yu, C., Dong, X., Zhang, X., Xue, M., ...and Fu, Y. (2012). Synthesis, characterization and photocatalytic activity of Cu-doped Zn/ZnO photocatalyst with carbon modification. *Journal of Materials Chemistry*, 22(45), 23780-23788.

[77] Shafique, M. A., Shah, S. A., Nafees, M., Rasheed, K., and Ahmad, R. (2012). Effect of doping concentration on absorbance, structural, and magnetic properties of cobalt-doped ZnO nano- crystallites. *International Nano Letters*, 2, 1-7.

[78] Wang, Y., Wang, Y., Jiang, R., and Xu, R. (2012). Cobalt phosphate–ZnO composite photocatalysts for oxygen evolution from photocatalytic water oxidation. *Industrial and engineering chemistry research*, 51(30), 9945-9951.

[79] Rongliang He, Rosalie K. Hocking, Takuya Tsuzuki, "Co-doped ZnO nanopowders: Location of cobalt and reduction in photocatalytic Activity", *Mater. Chem. Phys*., 132, 1035– 1040 (2012).

[80] Subash, B., Krishnakumar, B., Velmurugan, R., Swaminathan, M., andShanthi, M. (2012). Synthesis of Ce co-doped Ag–ZnO photocatalyst with excellent performance for NBB dye degradation under natural sunlight illumination. *Catalysis Science and Technology*, 2(11), 2319- 2326.

[81] Liu, L., Li, S., Zhuang, J., Wang, L., Zhang, J., Li, H., ...and Zhang, P. (2011). Improved selective acetone sensing properties of Co-doped ZnO nanofibers by electrospinning. *Sensors and actuators B: chemical*, 155(2), 782-788.

[82] Arshad, M., Azam, A., Ahmed, A. S., Mollah, S., andNaqvi, A. H. (2011). Effect of Co substitution on the structural and optical properties of ZnO nanoparticles synthesized by sol–gel route. *Journal of alloys and Compounds*, 509(33), 8378-8381.

[83] Nair, M. G., Nirmala, M., Rekha, K., andAnukaliani, A. (2011). Structural, optical, photo catalytic and antibacterial activity of ZnO and Co doped ZnO nanoparticles. *Materials letters*, 65(12), 1797-1800.

[84] Rasouli, S., andMoeen, S. J. (2011). Combustion synthesis of Co-doped zinc oxide nanoparticles using mixture of citric acid–glycine fuels. *Journal of Alloys and Compounds*, 509(5), 1915-1919

[85] Nirmala, M., andAnukaliani, A. (2011). Characterization of undoped and Co doped ZnO nanoparticles synthesized by DC thermal plasma method. *Physica B: Condensed Matter*, 406(4), 911-915

[86] Patil, A. B., Patil, K. R., andPardeshi, S. K. (2010). Ecofriendly synthesis and solar photocatalytic activity of S-doped ZnO. *Journal of Hazardous Materials*, 183(1-3), 315-323.

[87] Nakhate, G. G., Nikam, V. S., Kanade, K. G., Arbuj, S., Kale, B. B., andBaeg, J. O. (2010). Hydrothermally derived nanosized Ni-doped TiO2: a visible light driven photocatalyst for methylene blue degradation. *Materials Chemistry and Physics*, 124(2-3), 976-981.

[88] Yang, H., andNie, S. (2009). Preparation and characterization of Co-doped ZnO nanomaterials. *Materials Chemistry and Physics*, 114(1), 279-282.

[89] Wang, B., Xia, C., Iqbal, J., Tang, N., Sun, Z., Lv, Y., and Wu, L. (2009). Influences of Co doping on the structural, optical and magnetic properties of ZnO nanorods synthesized by hydrothermal route. *Solid State Sciences*, 11(8), 1419-1422.

[90] Djerdj, I., Garnweitner, G., Arčon, D., Pregelj, M., Jagličić, Z., andNiederberger, M. (2008). Diluted magnetic semiconductors: Mn/Co-doped ZnO nanorods as case study. *Journal of Materials Chemistry*, 18(43), 5208-5217.

[91] Lok, M. (2009). Coprecipitation. *Synthesis of solid catalysts*, 135-151

[92] Bader, N. A. B. I. L., Benkhayal, A. A., & Zimmermann, B. (2014). Co-precipitation as a sample preparation technique for trace element analysis: an overview. *Int. J. Chem. Sci*, *12*(2), 519-525.

[93] Lavina, B., Dera, P., & Downs, R. T. (2014). Modern X-ray diffraction methods in mineralogy and geosciences. *Reviews in Mineralogy and Geochemistry*, *78*(1), 1-31.

[94] Chirayil, C. J., Abraham, J., Mishra, R. K., George, S. C., & Thomas, S. (2017). Instrumental techniques for the characterization of nanoparticles. In *Thermal and rheological measurement techniques for nanomaterials characterization* (pp. 1-36). Elsevier.

[95] Bardeen, J., Slatt, F. J., & Hall, L. (1965). Photoconductivity Conf., vol. 146.

[96] Rocha, F. S., Gomes, A. J., Lunardi, C. N., Kaliaguine, S., & Patience, G. S. (2018). Experimental methods in chemical engineering: Ultraviolet visible spectroscopy—UV-Vis. *The Canadian Journal of Chemical Engineering*, *96*(12), 2512-2517.

[97] Titus, D., Samuel, E. J. J., & Roopan, S. M. (2019). Nanoparticle characterization techniques. In *Green synthesis, characterization and applications of nanoparticles* (pp. 303-319). Elsevier.

[98] Bajaj, N. S., & Joshi, R. A. (2021). Energy materials: fundamentals to applications. *Elsevier Science r, 3*, 61-82.

[99] Titus, D., Samuel, E. J. J., & Roopan, S. M. (2019). Nanoparticle characterization techniques. In *Green synthesis, characterization and applications of nanoparticles* (pp. 303-319). Elsevier.

[100] Pawel Olko, (2010), Radiat. Meas.,. 45, 506-511.

[101] https://microbenotes.com/scanning-electron-microscope-sem/

[102] Om Prakash Choudhary and Priyanka. (2017). Int.J.Curr.Microbiol.App.Sci., 5, 1877-1882.

[103] Makuła, P., Pacia, M., & Macyk, W. (2018). How to correctly determine the band gap energy of modified semiconductor photocatalysts based on UV–Vis spectra. *The journal of physical chemistry letters*, *9*(23), 6814-6817.

[104] Rana, S. B., Singh, R. P. P., & Arya, S. (2017). Structural, optical, magnetic and antibacterial study of pure and cobalt doped ZnO nanoparticles. *Journal of Materials Science: Materials in Electronics*, *28*, 2660-2672.